

# Efficient Numerical Schemes for a Two-Phase Hydrodynamical Model of Active Liquid Crystals and Solids

Xuelong Gu<sup>a</sup>, Guanghua Ji<sup>b</sup>, and Qi Wang<sup>a,\*</sup>

<sup>a</sup>*Department of Mathematics, University of South Carolina, Columbia, SC, 29208, USA*

<sup>b</sup>*Laboratory of Mathematics and Complex Systems (Ministry of Education), School of Mathematical Sciences, Beijing Normal University, Beijing 100875, P.R. China*

---

## Abstract

We propose several linear, fully decoupled numerical schemes with first- and second-order temporal accuracy for a novel  $\mathbf{Q}$ -tensor-based two-phase hydrodynamic model that describes the coupling of active nematic liquid crystal solutions with isotropic solid substrates. The model is derived from the generalized Onsager principle and includes nontrivial terms that contribute zero to the total free energy dissipation. We prove that the proposed decoupled linear schemes are thermodynamically consistent at the discrete level. In the passive limit, the SGE-BDF1 and SGE-PDG schemes are unconditionally energy stable, while the SGE-BDF2 scheme is energy stable with respect to a modified energy under a standard boundedness assumption and a sufficiently large stabilization parameter. We then perform extensive numerical simulations to investigate how activity and other model parameters affect active-nematic fluid–solid interactions. Finally, we analyze the physical mechanisms underlying the observed behaviors, providing deeper insight into the dynamics of soft, confined active nematic fluids.

*Keywords:* Active matter; Liquid-crystal; Liquid crystal-solid substrate interaction; Thermodynamical consistency; Energy-stable schemes;

---

## 1. Introduction

Active matter encompasses a broad class of systems composed of self-driven entities that consume energy to generate motion or mechanical stresses, giving rise to behaviors fundamentally distinct from those observed in passive matter systems. Examples range from collective dynamics in bacterial suspensions [1] to fish schools [2], aerial flocks [3, 4], and cytoskeleton dynamics [5, 6].

Among active matter systems, active liquid crystals represent a unique subclass in which self-propelled anisotropic particles exhibit liquid crystalline order [7]. These systems arise naturally in biology—for example, in microtubule bundles [5], cytoskeletal filaments driven by molecular motors [6], migrating cell layers [8, 9], and dense suspensions of microswimmers [10]. They also provide novel design principles for synthetic active materials with potential technological applications. Based on the direction of force couples, active liquid crystals are further classified as contractile (forces directed inward along the particle axis) or extensile (forces directed outward) [11].

The theoretical foundations of active liquid crystals build on decades of work in active matter physics. Key advances include Ramaswamy’s and Marchetti et al.’s development of hydrodynamic theories [11, 12], the Toner-Tu model, which establishes that long-range order

---

\*Corresponding author.

E-mail address: [qwang@math.sc.edu](mailto:qwang@math.sc.edu) (Q. Wang).

is possible in two-dimensional active systems [13], and the Vicsek model, which demonstrates order-disorder transitions in collections of self-propelled particles [14]. These frameworks, complemented by computational studies, have revealed phenomena such as spontaneous flow generation, turbulence-like chaotic states, and emergent collective motion resembling bacterial suspensions [1, 10] and cytoskeletal dynamics [5].

A particularly rich platform for exploring these behaviors is the active nematic droplet: a soft-confined mixture of active nematic liquid crystal and isotropic fluid. Early computational studies by Giomi et al. [15] demonstrated activity-driven elongation and interfacial instabilities, while later work by Doostmohammadi et al. [16] and Ruske et al. [17] explored defect dynamics and morphology in two and three dimensions.

Existing continuum descriptions of these systems extend passive liquid crystal hydrodynamics by incorporating activity as a perturbation [11, 18]. However, these formulations often lack a variational structure, limiting both their analytical tractability and the design of energy-stable numerical methods. To address this gap, in our recent work, we developed a binary phase-field model for the two-phase mixture of active liquid crystals and viscous fluids. The model is derived using the variational and generalized Onsager principles [19–21], ensuring energy dissipation in the absence of activity. This guarantees thermodynamic consistency, enables rigorous analysis, and facilitates the development of stable numerical algorithms. The resulting system couples an Allen–Cahn type equation for the nematic order parameter with incompressible Navier–Stokes equations for fluid motion. Given the strong nonlinear interactions among the hydrodynamic variables, the design of efficient and robust computational methods presents both a significant challenge and a promising opportunity.

In addition to immiscible mixtures of active liquid crystals and isotropic viscous fluids, another important class of two-phase systems has received relatively little attention: active liquid crystals interfaced with solid structures, either as inclusions or bounding substrates. Boundary anchoring is known to play a central role in dictating both the dynamics and the equilibrium configuration of liquid crystal systems. Past studies have examined such boundary effects, but analytical and computational limitations have restricted investigations to simple, regular geometries. To date, no systematic study has addressed the interaction between liquid crystals and arbitrarily shaped solid inclusions or liquid crystals confined within domains of arbitrary geometries.

Motivated by our continuum framework for active liquid crystal-viscous fluid mixtures, we propose a continuum model for active liquid crystals interfaced with solid substrates of arbitrary shape. Analogous to the droplet model, the new formulation is derived via the generalized Onsager principle, ensuring thermodynamic consistency. The solid phase is represented by a momentum balance equation with a large friction coefficient and a viscoelastic constitutive relation. Distinct phases are described by a phase-field variable  $\phi \in [0, 1]$ , in close analogy with hydrodynamic phase-field models for droplet systems. The continuum model is a bona fide extension of the phase field Navier-Stokes system for binary fluids (e.g., Allen-Cahn-Navier-Stokes or Cahn-Hilliard-Navier-Stokes equations). We note that when the activity is suppressed, the model reduces to a passive liquid crystal and solid substrate system.

A wide array of numerical strategies exist for components of the Cahn-Hilliard-Allen-Cahn (CH-AC) or Cahn-Hilliard-Navier-Stokes (CH-NS) systems. For incompressible Navier-Stokes equations, projection methods remain widely used [22–24]. Phase-field equations have been addressed through linear stabilization [25–27], convex splitting [28, 29], and quadratization-based approaches such as invariant energy quadratization (IEQ) [30–33] and scalar auxiliary variable (SAV) methods [34, 35]. More recently, the supplemental variable method (SVM) has been introduced as a general framework for constructing thermodynamically consistent approximations of energy-based models [36–38].

A central challenge in designing fully decoupled, second-order schemes lies in handling the

nonlinear coupling between phase-field variables and the velocity field. Yang [39] proposed a decoupling strategy using nonlocal auxiliary variables governed by ODEs, while SAV-type variants [40] provide related approaches. However, such methods typically preserve only a modified energy that is weakly connected to the original. In our earlier work [41], we clarified the essence of these techniques by reformulating the governing system into a generalized gradient flow with respect to a modified energy. Applying classical discretizations to this reformulation, with explicit implementation of the coefficient matrix, yields linearly implicit, decoupled schemes that dissipate the modified energy.

Building on this insight, we introduce a skew-gradient embedding (SGE) framework, which reformulates generalized dissipative systems with “zero-energy-contribution” (ZEC) terms into a generalized gradient flow structure with respect to the original energy. All ZEC terms are absorbed into a skew-symmetric coefficient matrix in the form of an exterior 2-form. This embedding permits classical discretizations with fully explicit treatment of ZEC terms, thereby leading to decoupled schemes. Crucially, because the reformulation preserves the original energy structure, we can design both original-energy-dissipative schemes either modified-energy-dissipative schemes that remain closely tied to the physical energy.

Within this framework, we develop three fully decoupled, linearly implicit time-integration schemes:

- SGE-BDF1, a first-order scheme rigorously proven to preserve the original energy dissipation law;
- SGE-BDF2, a second-order scheme that is energy-stable under additional solution regularity assumptions and requires a sufficiently large stabilization parameter;
- SGE-PDG, a second-order scheme based on the polarized discrete gradient method [42], which is unconditionally energy-stable without restrictive assumptions and requires only a mild stabilization condition. The SGE-PDG scheme dissipates a polarized energy that remains tightly connected to the physical energy.

These schemes enable efficient and accurate simulations of active nematic fluids across a broad range of activity and environmental parameters. The model incorporates two distinct activity parameters:

- $\xi$ , quantifying the effect of molecular activity on nematic ordering and elastic stress;
- $\chi$ , characterizing the contribution of activity to the total stress (active stress).

Substrate friction is introduced into the bulk momentum balance equation through a damping term  $-b\mathbf{v}$  to approximate the solid phase. In principle, the coefficient  $b$  should be allowed to vary spatially to reflect the spatial nonhomogeneity of the solid substrate.

The remainder of this paper is organized as follows. In §2, we review the model for active nematic liquid crystal droplets. In §3, we introduce the proposed numerical scheme, proving its stability in the absence of activity. In §4, we propose a rough description of the spatial discretization and its energy stability. §5 presents numerical convergence tests and showcases diverse hydrodynamic behaviors of active nematic droplets under various conditions.

## 2. Hydrodynamic Model for Two-Phase Active Liquid Crystals and Isotropic Solids

### 2.1. Notations

In this paper, we use the classical lowercase letters such as  $f, g$  to represent scalar fields, boldface lowercase letters  $\mathbf{u}, \mathbf{v}$  to denote vector fields; and boldface Greek letters  $\boldsymbol{\tau}$  or boldface

uppercase letters  $\mathbf{Q}$  to denote second-order tensor fields. Let  $\Omega \subset \mathbb{R}^d$  be a square computational domain, where  $d = 2$  or  $3$  denotes the spatial dimension, with boundary  $\partial\Omega$ . All of these variables depend on space and time  $(\mathbf{x}, t)$ . We define the dot or inner product between vectors by  $\mathbf{u} \cdot \mathbf{v} = \sum_{i=1}^d u_i v_i$  and the inner product between second order tensors by  $\mathbf{P} : \mathbf{Q} = \text{tr}(\mathbf{P}^\top \mathbf{Q}) = \sum_{i=1}^d \sum_{j=1}^d \mathbf{P}_{ij} \mathbf{Q}_{ij}$ , where  $(\bullet)^\top$  denotes the transpose of tensor  $(\bullet)$ .

For functions defined in  $\Omega$  spatially, we introduce the inner-products for scalar, vector, tensor fields, respectively, as follows,

$$(f, g) = \int_{\Omega} f g dx, \quad (\mathbf{u}, \mathbf{v}) = \int_{\Omega} \mathbf{u} \cdot \mathbf{v} dx, \quad (\mathbf{P}, \mathbf{Q}) = \int_{\Omega} \mathbf{P} : \mathbf{Q} dx,$$

with the induced norm,  $\|\bullet\| = \sqrt{(\bullet, \bullet)}$ . The divergence of second order tensor  $\boldsymbol{\tau}$  is defined componentwise by  $[\text{div}\boldsymbol{\tau}]_i = \partial_j \tau_{ij}$ . Here, we employ the Einstein summation convention by omitting the summation symbol when indices are repeated. This convention will be used throughout the paper.

We define the second-order symmetric tensor space,  $\mathcal{M}$ , and its trace-free subspace,  $\mathcal{M}_0$ , as follows:

$$\begin{aligned} \mathcal{M} &= \{\mathbf{M} \in \mathbb{R}^{d,d}, \mathbf{M} = \mathbf{M}^\top\}, \\ \mathcal{M}_0 &= \{\mathbf{Q} \in \mathbb{R}^{d,d}, \mathbf{Q} \in \mathcal{M}, \text{tr}(\mathbf{Q}) = 0\}. \end{aligned}$$

## 2.2. Governing system of equations

We consider a two-phase materials system in isothermal conditions consisting of an active nematic liquid crystal fluid and an isotropic solid substrate. The solid substrate is effectively modeled as a highly dissipative, viscoelastic fluid. The active nematic liquid crystal fluid is composed of active liquid crystal solutions, with mass density  $\rho_1$  and velocity  $\mathbf{v}_1$ , while the solid or effective very viscoelastic fluid is characterized by mass density  $\rho_2$  and velocity  $\mathbf{v}_2$ . To describe the mixture, we define the total mass density  $\rho = \rho_1 + \rho_2$  and introduce the mass-averaged velocity  $\mathbf{v} = \frac{\rho_1 \mathbf{v}_1 + \rho_2 \mathbf{v}_2}{\rho}$ . Here, we assume the two-phase system is incompressible so that  $\rho = \text{const}$  and  $\nabla \cdot \mathbf{v} = 0$ . The mass and momentum conservation take the form

$$\begin{cases} \rho \frac{\partial \mathbf{v}}{\partial t} = \nabla \cdot (\boldsymbol{\sigma} - \rho \mathbf{v} \mathbf{v}) - b(\phi) \mathbf{v}, \\ \nabla \cdot \mathbf{v} = 0, \end{cases} \quad (2.1)$$

where  $[\nabla \mathbf{v}]_{ij} = \partial_j v_i$  is the velocity gradient and  $\boldsymbol{\sigma}$  the total stress tensor, the mass fraction of the active component  $\phi = \frac{\rho_1}{\rho}$  is used to distinguish active nematic fluid from passive solid components,  $b(\phi) \geq 0$  is the drag coefficient taking a large value in the solid and zero value in the active liquid crystal region. Specifically,

- $\phi = 1$  corresponds to the region fully occupied by the active nematic fluid,
- $\phi = 0$  corresponds to the isotropic solid,
- $0 < \phi < 1$  represents the interface between the two phases.

Generally,  $\phi$  may depend on both spatial and temporal variables. In this work, we fix  $\phi$  as a prescribed spatially varying function  $\phi = \phi(\mathbf{x})$ , which defines the spatial distribution of the active nematic phase. The model is valid though even if we prescribe  $\phi$  as time-dependent as well.  $b(\phi) > 0$  is a friction coefficient. By choosing a large value for  $b$ , we model the solid as a very dissipative viscoelastic fluid, fully separated from the active liquid crystal.

To characterize the orientational order of active liquid crystals, we employ a second-order, symmetric and traceless tensor order parameter  $\mathbf{Q}$  [43, 44], perceived as the traceless component

of the second moment tensor of the orientation distribution probability function of liquid crystals. In two spatial dimensions,  $\mathbf{Q}$  is given by the uniaxial representation  $\mathbf{Q} = 2q (\hat{\mathbf{n}}\hat{\mathbf{n}}^T - \frac{1}{2}\mathbf{I})$ , where  $q$  denotes the scalar degree of nematic order and  $\hat{\mathbf{n}}$  is a unit vector field known as the director, representing the average local orientation of the active particles. In 3D,  $\mathbf{Q}$  is generally biaxial when flows or strong anchoring boundary conditions are present. We note that a 3-D uniaxial state only shows up in relaxed equilibrium states or strong uniaxial elongational flows in passive liquid crystals [45, 46].

Throughout this work, we focus on the following boundary conditions:

$$\mathbf{v}|_{\partial\Omega} = \mathbf{0}, \quad (2.2)$$

and

$$\mathbf{Q}|_{\partial\Omega} = \mathbf{Q}_D \text{ or } \partial_{\mathbf{n}}\mathbf{Q}|_{\partial\Omega} = 0, \quad (2.3)$$

where  $\mathbf{n}$  denotes the outward unit normal vector on  $\partial\Omega$ . In both case, the boundary condition is required to be compatible with the constraint  $\mathbf{Q} \in \mathcal{M}_0$ . These boundary conditions play a crucial role in the derivation of energy estimates and energy stability. Other boundary conditions, such as periodic boundary conditions, can be treated in a similar manner, and the corresponding conclusions can be extended accordingly.

Within domain  $\Omega$ , the Helmholtz free energy functional depends on the density of active particles and the nematic order, given by

$$F_\phi(\mathbf{Q}, \nabla\mathbf{Q}) = \int_{\Omega} f_\phi(\mathbf{Q}, \nabla\mathbf{Q}) d\mathbf{x},$$

where  $f_\phi(\cdot)$  denotes the free energy density. We define the total free energy, including the macroscopic kinetic energy and the Helmholtz free energy, by

$$F_\phi^{\text{total}}(\mathbf{v}, \mathbf{Q}, \nabla\mathbf{Q}) = \frac{\rho}{2} \|\mathbf{v}\|^2 + F_\phi(\mathbf{Q}, \nabla\mathbf{Q}). \quad (2.4)$$

Under isothermal conditions, the rate of energy dissipation is given by

$$\frac{dF_\phi^{\text{total}}}{dt} = \int_{\Omega} [\rho\mathbf{v} \cdot \mathbf{v}_t - \mathbf{H} : \mathbf{Q}_t - \hat{r}\hat{\mu}] d\mathbf{x} + \int_{\partial\Omega} \mathbf{n} \cdot \mathbf{h} ds, \quad (2.5)$$

where,  $\mathbf{H} = -\frac{\delta F_\phi^{\text{total}}}{\delta \mathbf{Q}}$  defines the molecule field conjugate to the nematic order tensor  $\mathbf{Q}$ ,  $\hat{r}$  is the number of active particles per unit time and unit volume,  $\hat{\mu}$  is the energy gain or generated per unit particle, the boundary energy flux is  $\mathbf{h}$ ,  $\mathbf{n}$  the unit outward normal, and

$$\mathbf{h} = (\sigma - \rho\mathbf{v}\mathbf{v} - p\mathbf{I}) \cdot \mathbf{v} + \frac{\partial F_\phi}{\partial \nabla\mathbf{Q}} : \mathbf{Q}_t. \quad (2.6)$$

In (2.5), the first term represents the change of the kinetic energy, the second encapsulates the change in free energy through identity  $\frac{dF_\phi}{dt} = \int_{\Omega} \mathbf{H} : \mathbf{Q}_t d\mathbf{x}$ , and the third term describes the energy reduction rate of the biological energy corresponding to the consumption of energy by active particles. In the theory, we set  $\hat{r}$  as a prescribed constant and treat  $\hat{\mu}$  as a fundamental active parameter.

By substituting (2.1) into (2.5), the first contribution becomes

$$\begin{aligned} \int_{\Omega} \rho\mathbf{v}\mathbf{v}_t d\mathbf{x} &= \int_{\Omega} \mathbf{v} \cdot \nabla \cdot (\sigma - \rho\mathbf{v}\mathbf{v}) - b(\phi)|\mathbf{v}|^2 d\mathbf{x}, \\ &= \int_{\Omega} -\nabla\mathbf{v} : (\sigma - \rho\mathbf{v}\mathbf{v}) - b(\phi)|\mathbf{v}|^2 d\mathbf{x} + \int_{\partial\Omega} \mathbf{v} \cdot (\sigma - \rho\mathbf{v}\mathbf{v}) \cdot \mathbf{n} ds. \end{aligned} \quad (2.7)$$

Notice that in the case of Dirichlet boundary conditions,  $\mathbf{v} = 0$  on the boundary, the last surface integration is zero; otherwise, one must retain the surface contribution to the total free energy dissipation.

In assessing the second contribution in (2.5), we introduce the corotational time derivative for tensor  $\mathbf{Q}$ :

$$\dot{\mathbf{Q}} = \mathbf{Q}_t + \mathbf{v} \cdot \nabla \mathbf{Q} + \mathbf{Q} \cdot \boldsymbol{\Omega} - \boldsymbol{\Omega} \cdot \mathbf{Q}. \quad (2.8)$$

where  $\mathbf{D} = \frac{1}{2}(\nabla \mathbf{v} + \nabla \mathbf{v}^\top)$  is the symmetric rate of strain tensor and  $\boldsymbol{\Omega} = \frac{1}{2}(\nabla \mathbf{v} - \nabla \mathbf{v}^\top)$  the antisymmetric vorticity tensor. Exploiting the symmetry of  $\mathbf{Q}, \mathbf{H}$  alongside the antisymmetry of  $\boldsymbol{\Omega}$  yields

$$\begin{aligned} \mathbf{H} : \mathbf{Q}_t &= \mathbf{H} : (\dot{\mathbf{Q}} - \mathbf{v} \cdot \nabla \mathbf{Q} - \mathbf{Q} \cdot \boldsymbol{\Omega} + \boldsymbol{\Omega} \cdot \mathbf{Q}) \\ &= \mathbf{H} : \dot{\mathbf{Q}} - \mathbf{H} : (\mathbf{v} \cdot \nabla \mathbf{Q}) - \nabla \mathbf{v} : (\mathbf{Q} \cdot \mathbf{H} - \mathbf{H} \cdot \mathbf{Q}) \end{aligned} \quad (2.9)$$

We then decompose the stress into three parts: the antisymmetric part of the stress  $\boldsymbol{\sigma}^a$ , the Ericksen stress  $\boldsymbol{\sigma}^e$ , and the symmetric stress  $\boldsymbol{\sigma}^s$ , respectively,

$$\begin{aligned} \boldsymbol{\sigma}^a &= \mathbf{Q} \cdot \mathbf{H} - \mathbf{H} \cdot \mathbf{Q}, \\ \boldsymbol{\sigma}^e &= f_\phi \mathbf{I} - \nabla \mathbf{Q} : \frac{\partial f}{\partial \nabla \mathbf{Q}}, \\ \boldsymbol{\sigma}^s &= \boldsymbol{\sigma} - \rho \mathbf{v} \mathbf{v} - \boldsymbol{\sigma}^e - \boldsymbol{\sigma}^a. \end{aligned} \quad (2.10)$$

Note that symmetry of  $\boldsymbol{\sigma}^s$  can be derived from [47] and the following Gibbs-Duhem relation

$$\nabla \cdot \boldsymbol{\sigma}^e = -\mathbf{H} : \nabla \mathbf{Q}. \quad (2.11)$$

Combining (2.5), (2.7), (2.8), (2.9), (2.10) and (2.11), we rewrite the time rate of change of the total free energy as follows [20, 47]:

$$\frac{dF_\phi^{\text{total}}}{dt} = - \int_{\Omega} [\mathbf{D} : \boldsymbol{\sigma}^s + \mathbf{H} : \dot{\mathbf{Q}} + b(\phi)|\mathbf{v}|^2 + \hat{r}\hat{\mu}] d\mathbf{x}. \quad (2.12)$$

Notice that this is an inner product between generalized fluxes ( $\mathbf{D}, \dot{\mathbf{Q}}, \hat{r}$ ) and the corresponding forces ( $\boldsymbol{\sigma}^s, \mathbf{H}, \hat{\mu}$ ). Since time parity of  $\mathbf{D}$  is different from other fluxes and time parity of  $\boldsymbol{\sigma}^s$  is different from other forces, we distinguish between the components of the fluxes that show the same behavior under time inversion as the dissipative conjugate forces or fluxes, and those that show the opposite behavior called reactive conjugate forces or fluxes. We denote the various components by superscripts “ $d$ ” and “ $r$ ”, respectively [20, 47].

Following the generalized Onsager principle, a set of constitutive equations for the dissipative currents is obtained [20, 47]

$$\begin{pmatrix} \sigma_{\alpha\beta}^{s,d} \\ \dot{Q}_{\alpha\beta}^d \\ \hat{r}^d \end{pmatrix} = \begin{pmatrix} 2\eta(\phi)\delta_{\alpha k}\delta_{\beta l} & 0 & 0 \\ 0 & \Gamma_{\mathbf{Q}}(\phi)\delta_{\alpha k}\delta_{\beta l} & \zeta_{10}(\phi)Q_{\alpha\beta} \\ 0 & \zeta_{10}(\phi)Q_{kl} & \lambda \end{pmatrix} \begin{pmatrix} D_{kl} \\ H_{kl} \\ \hat{\mu} \end{pmatrix}. \quad (2.13)$$

Here,  $\eta(\phi)$  denotes the shear viscosity. For thermodynamic consistency, the diagonal parameters  $\eta(\phi), \Gamma_{\mathbf{Q}}(\phi)$  must be non-negative. For fluxes of the opposite time parity, the antisymmetric mobility, i.e., the reactive terms are given by

$$\begin{pmatrix} \sigma_{\alpha\beta}^{s,r} \\ \dot{Q}_{\alpha\beta}^r \\ \hat{r}^r \end{pmatrix} = \begin{pmatrix} 0 & -\mathcal{A}_{\alpha\beta kl} & \mathcal{B}_{\alpha\beta} \\ \mathcal{A}_{\alpha\beta kl} & 0 & 0 \\ -\mathcal{B}_{kl} & 0 & 0 \end{pmatrix} \begin{pmatrix} D_{kl} \\ H_{kl} \\ \hat{\mu} \end{pmatrix}, \quad (2.14)$$

where

$$\begin{aligned}\mathcal{A}_{\alpha\beta kl} &= \frac{2a}{d}\delta_{\alpha k}\delta_{\beta l} + a(Q_{\alpha k}\delta_{\beta l} + \delta_{\alpha k}Q_{\beta l}) - 2aQ_{kl}(Q_{\alpha\beta} + \frac{1}{d}\delta_{\alpha\beta}) + \theta_1\delta_{kl}\delta_{\alpha\beta}, \\ \mathcal{B}_{\alpha\beta} &= \zeta_0(\phi) - \zeta_2\delta_{\alpha\beta}.\end{aligned}$$

We rewrite  $\zeta_{10}(\phi)\hat{\mu}$  as  $\xi(\phi)$ ,  $\zeta_0(\phi)\hat{\mu}$  as  $-\chi(\phi)$ , where  $\xi(\phi)$  and  $\chi(\phi)$  quantify the particle's activity via a linear dependence on  $\hat{\mu}$ . The positive (negative) value of  $\chi$  corresponds to extensile (contractile) particles [18, 48, 49].

Adopting the expressions for dissipative and reactive fluxes in the above constitutive equations, we summarize the governing system of equations for the two-phase system as follows:

$$\begin{cases} \rho(\mathbf{v}_t + \mathbf{v} \cdot \nabla \mathbf{v}) = \nabla \cdot (\boldsymbol{\sigma}^a + \boldsymbol{\sigma}^s) - \mathbf{H} : \nabla \mathbf{Q} - b(\phi)\mathbf{v}, \\ \nabla \cdot \mathbf{v} = 0, \\ \mathbf{Q}_t + \mathbf{v} \cdot \nabla \mathbf{Q} = \Gamma_{\mathbf{Q}}(\phi)\mathbf{H} + \mathbf{S} + \xi(\phi)\mathbf{Q}, \end{cases} \quad (2.15)$$

where,

$$\begin{aligned}\boldsymbol{\sigma}^a &= \mathbf{Q} \cdot \mathbf{H} - \mathbf{H} \cdot \mathbf{Q}, \\ \boldsymbol{\sigma}^s &= -p\mathbf{I} + 2\eta(\phi)\mathbf{D} - a(\mathbf{Q} \cdot \mathbf{H} + \mathbf{H} \cdot \mathbf{Q}) - \frac{2a}{d}\mathbf{H} + 2a(\mathbf{Q} : \mathbf{H})(\mathbf{Q} + \frac{1}{d}\mathbf{I}) - \chi(\phi)\mathbf{Q}, \\ \mathbf{S} &= \boldsymbol{\Omega} \cdot \mathbf{Q} - \mathbf{Q} \cdot \boldsymbol{\Omega} + a(\mathbf{Q} \cdot \mathbf{D} + \mathbf{D} \cdot \mathbf{Q}) + \frac{2a}{d}\mathbf{D} - 2a(\mathbf{D} : \mathbf{Q})(\mathbf{Q} + \frac{1}{d}\mathbf{I}),\end{aligned}$$

and  $p$  is the hydrostatic pressure.

We further decompose the Helmholtz free energy of the liquid crystal system into three components: the conformational entropy, bulk and anchoring energy as follows [44]

$$F_\phi(\mathbf{Q}, \nabla \mathbf{Q}) = F_{\text{el}}(\nabla \mathbf{Q}) + F_{\text{bulk}}(\mathbf{Q}) + F_{\text{anch}}(\mathbf{Q}). \quad (2.16)$$

The conformational entropy is given by

$$F_{\text{el}}(\nabla \mathbf{Q}) = \int_{\Omega} \frac{K(\phi)}{2} |\nabla \mathbf{Q}|^2 d\mathbf{x}, \quad (2.17)$$

where the coefficient  $K(\phi)$  depends on phase-field  $\phi$  and thus modulates the energetic penalty for spatial distortions of  $\mathbf{Q}$  according to the local material state. The bulk free energy takes the classical Landau-de Gennes form [44],

$$F_{\text{bulk}}(\mathbf{Q}) = \int_{\Omega} \left[ \frac{\alpha(\phi)}{2} \text{tr}(\mathbf{Q}^2) - \frac{\beta(\phi)}{3} \text{tr}(\mathbf{Q}^3) + \frac{\gamma(\phi)}{4} (\text{tr}(\mathbf{Q}^2))^2 \right] d\mathbf{x}, \quad (2.18)$$

where the coefficients depend on  $\phi$  through the functions,

$$\alpha(\phi) = A\left(1 - \frac{N(\phi)}{3}\right), \quad \beta(\phi) = \gamma(\phi) = AN(\phi).$$

Here,  $A > 0$  sets the bulk energy scale, and  $N(\phi) \geq 0$  is a scalar dimensionless concentration [17, 43, 50].

To model weak anchoring effects at the fluid-solid interface, the anchoring energy is proposed as follows

$$F_{\text{anch}}(\mathbf{Q}) = \int_{\Omega} \frac{W(\phi)}{2} |\mathbf{Q} - \mathbf{Q}_\star|^2 d\mathbf{x}, \quad (2.19)$$

where  $W(\phi) = W_0|\nabla\phi|$  localizes the anchoring contribution to the interfacial region of finite thickness,  $W_0$  parameterizes the anchoring strength, and  $\mathbf{Q}_\star$  represents the preferred configuration imposed by the boundary anchoring (a traceless second order tensor).

**Remark 2.1** The governing system of equations is derived for the two-phase active liquid crystal solutions and highly dissipative, viscoelastic fluid system. We use the highly dissipative viscoelastic fluid part to describe the isotropic solid approximately by enforcing a large friction term  $-b(\phi)\mathbf{v}$ , assuming a large viscosity coefficient, specifying other viscoelastic materials parameters, and annihilating active parameters.  $\mathbf{Q}_*$  denotes a prescribed, three-dimensional, anchored  $\mathbf{Q}$ -tensor field, which admits a uniaxial form,

$$\mathbf{Q}_* = S_{eq}(\mathbf{p}\mathbf{p}^\top - \frac{1}{3}\mathbf{I}), \quad (2.20)$$

where  $\mathbf{p}$  is a unit vector representing the preferred molecular orientation at the interface. In this study,  $\mathbf{p}$  corresponds to the unit outward normal vector in the case of normal anchoring, or to the unit tangential vector along the solid boundary in the case of tangential anchoring.

Under conditions  $\alpha < 0$  and  $\beta, \gamma < 0$ ,

$$S_{eq} = \frac{\beta + \sqrt{\beta^2 - 24\alpha\gamma}}{4\gamma}.$$

This uniaxial equilibrium structure and the expression for  $S_{eq}$  are standard results in the Landau–Genes theory for nematic liquid crystals; see, for example, [44] for a details.

We introduce characteristic length scale  $l_0$  and time scale  $t_0$  to nondimensionize the physical variables as follows

$$\tilde{t} = \frac{t}{t_0}, \quad \tilde{\mathbf{x}} = \frac{\mathbf{x}}{l_0}, \quad \tilde{\mathbf{H}} = \frac{t_0^2 \mathbf{H}}{\rho l_0^2}. \quad (2.21)$$

Then, the following dimensionless parameters arise

$$\tilde{A} = \frac{t_0^2 A}{\rho l_0^2}, \quad \tilde{\Gamma}_{\mathbf{Q}} = \frac{\rho l_0^2 \Gamma_{\mathbf{Q}}}{t_0}, \quad \tilde{K} = \frac{t_0^2 K}{\rho}, \quad \tilde{a} = a, \quad \tilde{\eta} = \frac{t_0 \eta}{\rho l_0^2}, \quad \tilde{p} = \frac{t_0^2 p}{\rho l_0^2}, \quad \tilde{\xi} = t_0 \xi, \quad \tilde{\chi} = \frac{t_0^2 \chi}{\rho l_0^2}. \quad (2.22)$$

Utilizing (2.21) and (2.22), we obtain the dimensionless governing equations after dropping the  $\sim$  over the parameters:

$$\begin{cases} \mathbf{v}_t + \mathbf{v} \cdot \nabla \mathbf{v} = -\nabla p + 2\nabla \cdot (\eta(\phi)\mathbf{D}) + \nabla \cdot \boldsymbol{\Sigma} - \mathbf{H} : \nabla \mathbf{Q} - \nabla \cdot (\chi(\phi)\mathbf{Q}) - b(\phi)\mathbf{v}, \\ \nabla \cdot \mathbf{v} = 0, \\ \mathbf{Q}_t + \mathbf{v} \cdot \nabla \mathbf{Q} = \Gamma_{\mathbf{Q}}(\phi)\mathbf{H} + \mathbf{S} + \xi(\phi)\mathbf{Q}, \\ \boldsymbol{\Sigma} = \mathbf{Q} \cdot \mathbf{H} - \mathbf{H} \cdot \mathbf{Q} - a(\mathbf{Q} \cdot \mathbf{H} + \mathbf{H} \cdot \mathbf{Q}) - \frac{2a}{d}\mathbf{H} + 2a(\mathbf{Q} : \mathbf{H})(\mathbf{Q} + \frac{1}{d}\mathbf{I}), \\ \mathbf{S} = \boldsymbol{\Omega} \cdot \mathbf{Q} - \mathbf{Q} \cdot \boldsymbol{\Omega} + a(\mathbf{Q} \cdot \mathbf{D} + \mathbf{D} \cdot \mathbf{Q}) + \frac{2a}{d}\mathbf{D} - 2a(\mathbf{D} : \mathbf{Q})(\mathbf{Q} + \frac{1}{d}\mathbf{I}), \\ \mathbf{H} = \nabla \cdot (K(\phi)\nabla \mathbf{Q}) - \left[ \alpha(\phi)\mathbf{Q} - \beta(\phi)(\mathbf{Q}^2 - \frac{\text{tr}(\mathbf{Q}^2)}{d}\mathbf{I}) + \gamma(\phi)\text{tr}(\mathbf{Q}^2)\mathbf{Q} \right] - W(\phi)(\mathbf{Q} - \mathbf{Q}_*), \end{cases} \quad (2.23)$$

In this study, we prescribe the model parameters in (2.23) as follows:

$$\begin{aligned} b(\phi) &= b_{solid}(1 - \phi), \quad \eta(\phi) = \eta_{fluid}\phi + \eta_{solid}(1 - \phi), \\ \xi(\phi) &= \xi_{fluid}\phi, \quad \chi(\phi) = \chi_{fluid}\phi, \quad K(\phi) = K_{fluid}\phi, \\ N(\phi) &= N_{fluid}\phi + N_{solid}(1 - \phi), \quad \Gamma_{\mathbf{Q}} = \Gamma_{fluid}\phi + \Gamma_{solid}(1 - \phi). \end{aligned} \quad (2.24)$$

Here, the  $(\bullet)_{fluid}$  and  $(\bullet)_{solid}$  are prescribed model parameters in the active liquid crystal fluid and solid, respectively.

The total free energy of (2.23) is given by

$$F_\phi^{\text{total}}(\mathbf{v}, \mathbf{Q}, \nabla \mathbf{Q}) = \frac{\rho}{2} \|\mathbf{v}\|^2 + F_\phi(\mathbf{Q}, \nabla \mathbf{Q}). \quad (2.25)$$

It yields following energy dissipation rate:

$$\frac{dF_\phi^{total}}{dt} = - \int_{\Omega} [2\eta(\phi)|\mathbf{D}|^2 + \Gamma(\phi)|\mathbf{H}|^2 + b(\phi)|\mathbf{v}|^2] d\mathbf{x} + (\mathbf{Q}, \chi(\phi)\mathbf{D} - \xi(\phi)\mathbf{H}). \quad (2.26)$$

If active parameters  $\chi(\phi)$ ,  $\xi(\phi)$  vanish, we have  $\frac{dF_\phi^{total}}{dt} \leq 0$ . In this case, the governing system (2.23) describes a two-phase system consisting of passive liquid crystals and solids whose total free energy dissipative.

**Remark 2.2** Note that  $\mathbf{H}$  corresponds to the variational derivative in subspace  $\mathcal{M}_0$ . Specifically,  $\mathbf{H} = -\mathcal{P}_{\mathcal{M}_0} \frac{\delta F_\phi^{total}}{\delta \mathbf{Q}}$ , where  $\mathcal{P}_{\mathcal{M}_0}$  is the orthogonal projection operator from  $\mathcal{M}$  to  $\mathcal{M}_0$ , given by

$$\mathcal{P}_{\mathcal{M}_0}(\mathbf{M}) = \mathbf{M} - \frac{1}{d} \text{tr}(\mathbf{M}).$$

### 3. Thermodynamically consistent, decoupled, and linearly implicit numerical algorithms

In this section, we present several thermodynamically consistent discretizations of system (2.23), i.e., the resulting numerical schemes preserve a discrete analog of (2.26). In particular, when the liquid crystal system is passive, the proposed algorithms preserve the discrete energy dissipation rate, leading to energy stability. We remark that the energy dissipation rate preservation is stronger property than simply energy stability.

#### 3.1. SGE reformulation of the system

We reformulate (2.23) using SGE formulated in [41]. The central idea of the SGE approach is to express the “zero-energy-contribution” (ZEC) term in a low-rank skew-gradient form. By unveiling this intrinsic gradient structure, one can seamlessly adapt classical techniques to construct energy dissipation rate preserving or energy stable schemes.

We define the following intermediate variables:

$$\begin{aligned} \mathbf{g}_v &= \mathbf{v}, & \mathbf{c}_v &= -\mathbf{v} \cdot \nabla \mathbf{v} + \nabla \cdot \Sigma - \mathbf{Q} : \nabla \mathbf{H}, & \mathbf{f}_v &= -\nabla \cdot (\chi(\phi)\mathbf{Q}), \\ \mathbf{G}_Q &= -\mathbf{H}, & \mathbf{C}_Q &= -\mathbf{v} \cdot \nabla \mathbf{Q} + \mathbf{S}, & \mathbf{F}_Q &= \xi(\phi)\mathbf{Q}, \end{aligned}$$

Then, (2.23) can be recast into

$$\begin{cases} \mathbf{v}_t = -\nabla p + 2\nabla \cdot (\eta(\phi)\mathbf{D}) - b(\phi)\mathbf{v} + \frac{(\mathbf{g}_v, \mathbf{g}_v) + (\mathbf{G}_Q, \mathbf{G}_Q)}{\mathcal{G}(\mathbf{g}_v, \mathbf{G}_Q)} \mathbf{c}_v - \frac{(\mathbf{g}_v, \mathbf{c}_v) + (\mathbf{G}_Q, \mathbf{C}_Q)}{\mathcal{G}(\mathbf{g}_v, \mathbf{G}_Q)} \mathbf{g}_v + \mathbf{f}_v, \\ \nabla \cdot \mathbf{v} = 0, \\ \mathbf{Q}_t = \Gamma_Q(\phi)\mathbf{H} + \frac{(\mathbf{g}_v, \mathbf{g}_v) + (\mathbf{G}_Q, \mathbf{G}_Q)}{\mathcal{G}(\mathbf{g}_v, \mathbf{G}_Q)} \mathbf{C}_Q - \frac{(\mathbf{g}_v, \mathbf{c}_v) + (\mathbf{G}_Q, \mathbf{C}_Q)}{\mathcal{G}(\mathbf{g}_v, \mathbf{G}_Q)} \mathbf{G}_Q + \mathbf{F}_Q. \end{cases}, \quad (3.1)$$

where

$$\mathcal{G}(\mathbf{g}_v, \mathbf{G}_Q) = \|\mathbf{g}_v\|^2 + \|\mathbf{G}_Q\|^2. \quad (3.2)$$

Note that the SGE reformulation, (3.1), is equivalent to the original system, (2.23), via the following identities

$$\begin{cases} (\mathbf{g}_v, \mathbf{g}_v) + (\mathbf{G}_Q, \mathbf{G}_Q) = \mathcal{G}(\mathbf{g}_v, \mathbf{G}_Q), \\ (\mathbf{g}_v, \mathbf{c}_v) + (\mathbf{G}_Q, \mathbf{C}_Q) = 0. \end{cases} \quad (3.3)$$

For the second identity, readers please refer to [51] for details.

**Remark 3.1** Note that  $\mathcal{G}(\mathbf{g}_v, \mathbf{G}_Q)$  is defined as the sum of the squared  $L^2$  norms of the free-energy gradient components (3.2). The condition  $\mathcal{G}(\mathbf{g}_v, \mathbf{G}_Q) = 0$  therefore corresponds to the system reaching a critical point on the energy surface. Away from such critical points, one generally has  $\mathcal{G}(\mathbf{g}_v, \mathbf{G}_Q) \neq 0$ . To ensure that the formulation remains well defined in both situations, the degenerate case is treated in a manner consistent with the general case: if  $(\mathbf{g}_v, \mathbf{G}_Q) = 0$ , the coefficients in front of  $\mathbf{c}_v, \mathbf{C}_Q$  are set to 1, while those multiplying  $\mathbf{g}_v$  and  $\mathbf{G}_Q$  are set to 0. Since the main difficulty in constructing an energy-stable scheme arises in the case where the free-energy gradient does not vanish, i.e.,  $\mathcal{G}(\mathbf{g}_v, \mathbf{G}_Q) \neq 0$ , we primarily focus on this regime in the subsequent analysis.

**Remark 3.2** By introducing  $\Psi = (\mathbf{v}, \mathbf{Q})$ , system (3.1) can be further written in the form,

$$\Psi_t = \mathcal{M}(\Psi)\delta_{\Psi}F^{total} + \mathcal{J}(\Psi)\delta_{\Psi}F^{total} + \mathcal{F}(\Psi),$$

where  $\delta_{\Psi}$  denotes the variational derivative of the total energy functional with respect to  $\Psi$  in space  $\mathbf{V} \times \mathcal{M}_0$ . For velocity fields subject to the zero Dirichlet boundary condition, the admissible solution space is defined as  $\mathbf{V} = \{\mathbf{v} \in [L^2(\Omega)]^d | \nabla \cdot \mathbf{v} = 0, \mathbf{v} \cdot \mathbf{n}|_{\partial\Omega} = 0\}$ . The specific forms of the operators are given by

$$\mathcal{M}(\Psi) = \text{diag}(\mathcal{B}, -\Gamma_Q), \quad \mathcal{J}(\Psi) = \begin{pmatrix} \mathbf{v} \\ -\mathbf{H} \end{pmatrix} \wedge \begin{pmatrix} \mathcal{P}_V \mathbf{c}_v \mathcal{P}_V \\ \mathcal{P}_{\mathcal{M}_0} \mathbf{C}_Q \mathcal{P}_{\mathcal{M}_0} \end{pmatrix}, \quad \mathcal{F}(\Psi) = \begin{pmatrix} \mathcal{P}_V \mathbf{f}_v \\ \mathbf{F}_Q \end{pmatrix}. \quad (3.4)$$

Here,  $\delta_{\Psi}F^{total} = (\mathbf{v}, -\mathbf{H}) = (\mathbf{g}_v, \mathbf{G}_Q)$ ,  $\mathcal{P}_V$  denotes the Hemholtz-Leray projection, and  $\mathcal{B} = \mathcal{P}_V \nabla \cdot (\nabla(\bullet))$ , represents a Stokes operator with variable coefficients. It is self-adjoint with non-positive spectra when  $\eta > 0$ , ensuring that  $\mathcal{M}$  is a self-adjoint and non-positive mobility operator. The operator  $\mathcal{J}(\Psi)$  defines a skew-symmetric operator on  $\mathbf{V} \times \mathcal{M}_0$  and therefore generates the reversible part of the dynamics, contributing zero dissipation to the total free energy, as shown in our previous work [41]. This is an activity-driven gradient flow system, where  $\mathcal{F}(\Psi)$  represents the generalized force due to the activity.

The reformulation, (3.4), together with its equivalent form (3.1), provides a convenient framework for constructing energy-stable schemes using some well-tested tools, such as stabilization techniques [52–56], and discrete gradient methods [57–61]. In addition, since all convective terms are encapsulated within operator  $\mathcal{J}(\Psi)$ , they can be discretized explicitly independent of the spatial discretization without destroying the underlying energy dissipative structure. Notably, the resulting system can also be solved efficiently in a fully decoupled manner due to the low-rank (rank-2) structure in  $\mathcal{J}(\Psi)$ .

### 3.2. First and second-order schemes based on stabilization techniques

In this section, we construct first- and second-order numerical schemes based on the stabilization technique and the SGE reformulation of governing system (3.1). By applying these two techniques, we break down the discretized, coupled hydrodynamic system into decoupled systems: a Stokes problem for the velocity-pressure pair and a sequence of decoupled Poisson equations. Each time step thus requires only a Stokes solver and a Poisson solver, respectively, greatly simplifying the overall computation.

Suppose we consider the problem over time interval  $(0, T]$ . Let  $N_t$  be a positive integer representing the total number of time steps. We partition the interval into a uniform temporal grid with time step size  $\tau = \frac{T}{N_t}$ . The discrete time levels are denoted by  $t_n = n\tau$  for  $n = 0, 1, \dots, N_t$ , and the approximation of a physical variable  $f$  at time  $t_n$  is denoted by  $f^n$ .

We next introduce stabilized backward-difference schemes of first and second order (SGE-BDF1 and SGE-BDF2) for (3.1), respectively. At each time step the update takes the unified

form as follows,

$$\begin{cases} \frac{\alpha_k \mathbf{v}^{n+1} - A_k(\mathbf{v}^n)}{\tau} = -\nabla p^{n+1} + 2\nabla \cdot (\eta \mathbf{D}^{n+1}) - b\mathbf{v}^{n+1} + \zeta^{n+1} B_k(\mathbf{c}_v^n) - \omega^{n+1} B_k(\mathbf{g}_v^n) + B_k(\mathbf{f}_v^n), \\ \nabla \cdot \mathbf{v}^{n+1} = 0, \\ \frac{\alpha_k \mathbf{Q}^{n+1} - A_k(\mathbf{Q}^n)}{\tau} = \Gamma_{\mathbf{Q}} \mathbf{H}^{n+1} + \zeta^{n+1} B_k(\mathbf{C}_{\mathbf{Q}}^n) - \omega^{n+1} B_k(\mathbf{G}_{\mathbf{Q}}^n) + B_k(\mathbf{F}_{\mathbf{Q}}^n), \\ \zeta^{n+1} = \frac{(\mathbf{g}_v^{n+1}, B_k(\mathbf{g}_v^n)) + (\mathbf{G}_{\mathbf{Q}}^{n+1}, B_k(\mathbf{G}_{\mathbf{Q}}^n))}{\mathcal{G}(B_k(\mathbf{g}_v^n), B_k(\mathbf{G}_{\mathbf{Q}}^n))}, \quad \omega^{n+1} = \frac{(\mathbf{g}_v^{n+1}, B_k(\mathbf{c}_v^n)) + (\mathbf{G}_{\mathbf{Q}}^{n+1}, B_k(\mathbf{C}_{\mathbf{Q}}^n))}{\mathcal{G}(B_k(\mathbf{g}_v^n), B_k(\mathbf{C}_{\mathbf{Q}}^n))}, \end{cases} \quad (3.5)$$

where  $k = 1$  yields the first-order scheme and  $k = 2$  the second-order variant, The weights  $\alpha_k$ ,  $A_k$  and  $B_k$  arise from a Taylor expansion and are specified as follows:

- SGE-BDF1 (first-order,  $k = 1$ ):  $\alpha_1 = 1$ ,  $A_1(f^n) = f^n$ ,  $B_1(f^n) = f^n$ ,
- SGE-BDF2 (second-order,  $k = 2$ ):  $\alpha_2 = \frac{3}{2}$ ,  $A_2(f^n) = 2f^n - \frac{1}{2}f^{n-1}$ ,  $B_2(f^n) = 2f^n - f^{n-1}$ .

In addition, we set  $\mathbf{G}_{\mathbf{Q}}^{n+1} = -\mathbf{H}^{n+1}$  with

$$\mathbf{H}^{n+1} = \begin{cases} \nabla \cdot (K \nabla \mathbf{Q}^{n+1}) - W(\mathbf{Q}^{n+1} - \mathbf{Q}_*) - \kappa(\mathbf{Q}^{n+1} - \mathbf{Q}^n) - f_{\text{bulk}}(\mathbf{Q}^n), & \text{(first-order),} \\ \nabla \cdot (K \nabla \mathbf{Q}^{n+1}) - W(\mathbf{Q}^{n+1} - \mathbf{Q}_*) - \tau \kappa (\alpha_2 \mathbf{Q}^{n+1} - A_2(\mathbf{Q}^n)) - B_2(f_{\text{bulk}}(\mathbf{Q}^n)), & \text{(second-order).} \end{cases} \quad (3.6)$$

At first glance, (3.5) appears only weakly coupled-through parameters  $\zeta^{n+1}$  and  $\omega^{n+1}$ -despite being linearly implicit. In the next section, we show that the update can in fact be carried out in two fully decoupled steps, eliminating any potential coupling.

By inspecting linear system (3.5) and formulation (3.6) at time level  $n + 1$ , we split each unknown into three independent components

$$\begin{cases} \mathbf{v}^{n+1} = \mathbf{v}_1 + \zeta^{n+1} \mathbf{v}_2 - \omega^{n+1} \mathbf{v}_3, \\ \mathbf{Q}^{n+1} = \mathbf{Q}_1 + \zeta^{n+1} \mathbf{Q}_2 - \omega^{n+1} \mathbf{Q}_3, \\ \mathbf{H}^{n+1} = \mathbf{H}_1 + \zeta^{n+1} \mathbf{H}_2 - \omega^{n+1} \mathbf{H}_3, \end{cases} \quad (3.7)$$

Each triplet  $(\mathbf{v}_i, \mathbf{Q}_i, \mathbf{H}_i)$  is then computed from fully decoupled subproblems:

- **Generalized Stokes equations.** For  $i = 1, 2, 3$ , find  $\mathbf{v}_i$  by solving:

$$\begin{cases} \left( \frac{\alpha_k}{\tau} + b \right) \mathbf{v}_i^{n+1} - 2\nabla \cdot (\eta \mathbf{D}(\mathbf{v}_i^{n+1})) + \nabla p^{n+1} = \mathbf{f}_i, \\ \nabla \cdot \mathbf{v}_i^{n+1} = 0. \end{cases} \quad (3.8)$$

- **Decoupled tensor Poisson equations.** For  $i = 1, 2, 3$ , find  $\mathbf{Q}_i$  from

$$\left( \frac{\alpha_k}{\tau} + \Gamma_{\mathbf{Q}}(\kappa + W) \right) \mathbf{Q}_i^{n+1} - \Gamma_{\mathbf{Q}} \nabla \cdot (K \nabla \mathbf{Q}_i^{n+1}) = \mathbf{F}_i. \quad (3.9)$$

The right-hand sides contain all explicit terms:

$$\begin{cases} \mathbf{f}_1 = \frac{1}{\tau} A_k(\mathbf{v}^n) + B_k(\mathbf{f}_v^n), \quad \mathbf{f}_2 = B_k(\mathbf{c}_v^n), \quad \mathbf{f}_3 = B_k(\mathbf{g}_v^n), \\ \mathbf{F}_1 = \frac{1}{\tau} A_k(\mathbf{Q}^n) + B_k(\mathbf{F}_{\mathbf{Q}}^n), \quad \mathbf{F}_2 = B_k(\mathbf{C}_{\mathbf{Q}}^n), \quad \mathbf{F}_3 = B_k(\mathbf{G}_{\mathbf{Q}}^n). \end{cases}$$

Next, each  $\mathbf{H}_i^{n+1}$  is obtained by substituting (3.7) into (3.6) and collecting like terms with respect to  $\zeta^{n+1}$  and  $\omega^{n+1}$ . As an example, for the SGE-BDF1 scheme, this reads

$$\begin{cases} \mathbf{H}_1^{n+1} = \nabla \cdot (K \nabla \mathbf{Q}_1^{n+1}) - W(\mathbf{Q}_1^{n+1} - \mathbf{Q}_*) - \kappa(\mathbf{Q}_1^{n+1} - \mathbf{Q}^n) - f_{\text{bulk}}(\mathbf{Q}^n), \\ \mathbf{H}_2^{n+1} = \nabla \cdot (K \nabla \mathbf{Q}_2^{n+1}) - (W + \kappa) \mathbf{Q}_2^{n+1}, \\ \mathbf{H}_3^{n+1} = \nabla \cdot (K \nabla \mathbf{Q}_3^{n+1}) - (W + \kappa) \mathbf{Q}_3^{n+1}. \end{cases}$$

To close the time step, we solve for the two scalars  $\zeta^{n+1}$  and  $\omega^{n+1}$ . Noting that  $\mathbf{G}_Q^{n+1} = -\mathbf{H}^{n+1}$  and letting  $\mathbf{G}_i = -\mathbf{H}_i$ , we take the inner-product of the velocity split in (3.7) with  $B_k(\mathbf{g}_v^n)$  and  $B_k(\mathbf{c}_v^n)$ , and of the  $\mathbf{Q}$ -split (3.7) with  $-B_k(\mathbf{G}_Q^n)$  and  $-B_k(\mathbf{C}_Q^n)$ . This produces four equations:

$$\begin{aligned} (\mathbf{g}_v^{n+1}, B_k(\mathbf{g}_v^n)) &= (\mathbf{v}_1, B_k(\mathbf{g}_v^n)) + \zeta^{n+1}(\mathbf{v}_2, B_k(\mathbf{g}_v^n)) - \omega^{n+1}(\mathbf{v}_3, B_k(\mathbf{g}_v^n)), \\ (\mathbf{g}_v^{n+1}, B_k(\mathbf{c}_v^n)) &= (\mathbf{v}_1, B_k(\mathbf{c}_v^n)) + \zeta^{n+1}(\mathbf{v}_2, B_k(\mathbf{c}_v^n)) - \omega^{n+1}(\mathbf{v}_3, B_k(\mathbf{c}_v^n)), \\ (\mathbf{G}_Q^{n+1}, B_k(\mathbf{G}_Q^n)) &= (\mathbf{G}_1, B_k(\mathbf{G}_Q^n)) + \zeta^{n+1}(\mathbf{G}_2, B_k(\mathbf{G}_Q^n)) - \omega^{n+1}(\mathbf{G}_3, B_k(\mathbf{G}_Q^n)), \\ (\mathbf{G}_Q^{n+1}, B_k(\mathbf{C}_Q^n)) &= (\mathbf{G}_1, B_k(\mathbf{C}_Q^n)) + \zeta^{n+1}(\mathbf{G}_2, B_k(\mathbf{C}_Q^n)) - \omega^{n+1}(\mathbf{G}_3, B_k(\mathbf{C}_Q^n)). \end{aligned} \quad (3.10)$$

By summing the first and third equations-and likewise the second and fourth-in (3.10) to eliminate two unknowns  $(\mathbf{v}_v, \mathbf{G}_Q)$ , we arrive at the following  $2 \times 2$  systems for  $\zeta^{n+1}$ ,  $\omega^{n+1}$ :

$$\begin{cases} [\mathcal{G}(B_k(\mathbf{g}_v^n), B_k(\mathbf{G}_Q^n)) - (\mathbf{v}_2, B_k(\mathbf{g}_v^n)) - (\mathbf{G}_2, B_k(\mathbf{G}_Q^n))] \zeta^{n+1} + [(\mathbf{v}_3, B_k(\mathbf{g}_v^n)) + (\mathbf{G}_3, B_k(\mathbf{G}_Q^n))] \omega^{n+1} \\ \quad = (\mathbf{v}_1, B_k(\mathbf{g}_v^n)) + (\mathbf{G}_1, B_k(\mathbf{G}_Q^n)), \\ [(\mathbf{v}_2, B_k(\mathbf{c}_v^n)) + (\mathbf{G}_2, B_k(\mathbf{C}_Q^n))] \zeta^{n+1} - [\mathcal{G}(B_k(\mathbf{g}_v^n), B_k(\mathbf{G}_Q^n)) + (\mathbf{v}_2, B_k(\mathbf{c}_v^n)) + (\mathbf{G}_2, B_k(\mathbf{C}_Q^n))] \omega^{n+1} \\ \quad = -(\mathbf{v}_1, B_k(\mathbf{c}_v^n)) - (\mathbf{G}_1, B_k(\mathbf{C}_Q^n)). \end{cases} \quad (3.11)$$

For sufficiently small time steps, the determinant of the coefficient matrix in system (3.11) is nonzero, and hence system (3.11) admits a unique solution for  $\zeta^{n+1}$  and  $\omega^{n+1}$ . Substituting them back into the decompositions, (3.7), yields solutions  $\mathbf{v}^{n+1}$  and  $\mathbf{Q}^{n+1}$  at the next time level.

Notice that at each time step, the update decouples into just three Stokes type equations, multiple scalar Poisson equations, and a single  $2 \times 2$  linear system. These yield a linearly implicit, fully decoupled system in which equations arising at each time step can be solved efficiently.

We now turn to the method's structure-preserving property. First, we note that if the initial  $\mathbf{Q}$ -tensor is traceless, this property is exactly retained at each subsequent time.

**Theorem 3.1** Suppose the initial condition  $\mathbf{v}_0$  and  $\mathbf{Q}_0$  satisfies  $\nabla \cdot \mathbf{v}_0 = 0$  and  $\text{tr}(\mathbf{Q}_0) = 0$ , then for any  $n = 1, \dots, N_t$ , solutions  $\mathbf{Q}^n$  solved from (3.5) satisfies  $\text{tr}(\mathbf{Q}^n) = 0$ .

*Proof.* We prove it by induction. Assume  $\text{tr}(\mathbf{Q}^0) = 0$ . For the SGE-BDF2 scheme, we also assume that the computed  $\mathbf{Q}^1$  is traceless. Now, suppose that for any  $1 \leq i \leq n$ , the sequence  $\{\mathbf{Q}^i\}_{i=1}^n$  solved from (3.5) satisfies  $\text{tr}(\mathbf{Q}^i) = 0$ . We next prove  $\text{tr}(\mathbf{Q}^{n+1}) = 0$ . Applying the trace operator on the third equation of (3.5) leads to

$$\frac{\alpha_k}{\tau} \text{tr}(\mathbf{Q}^{n+1}) = \Gamma_Q \text{tr}(\mathbf{H}^{n+1}) + \zeta^{n+1} \text{tr}(B_k(\mathbf{C}_Q^n)) - \omega^{n+1} \text{tr}(B_k(\mathbf{G}_Q^n)) + \text{tr}(B_k(\mathbf{F}_Q^n)). \quad (3.12)$$

Since  $B_k$  is linear, it follows immediately that

$$\text{tr}(B_k(\mathbf{C}_Q^n)) = B_k(\text{tr}(\mathbf{C}_Q^n)), \quad \text{tr}(B_k(\mathbf{G}_Q^n)) = B_k(\text{tr}(\mathbf{G}_Q^n)), \quad \text{tr}(B_k(\mathbf{F}_Q^n)) = B_k(\text{tr}(\mathbf{F}_Q^n)).$$

We first show that

$$\text{tr}(B_k(\mathbf{C}_Q^n)) = \text{tr}(B_k(\mathbf{G}_Q^n)) = \text{tr}(B_k(\mathbf{F}_Q^n)) = 0. \quad (3.13)$$

To do this, it suffices to prove

$$\text{tr}(\mathbf{C}_Q^n) = \text{tr}(\mathbf{G}_Q^n) = \text{tr}(\mathbf{F}_Q^n) = 0$$

by induction, which immediately implies (3.13) for the case  $k = 1$ . For  $k = 2$ , one also needs to verify

$$\text{tr}(\mathbf{C}_Q^{n-1}) = \text{tr}(\mathbf{G}_Q^{n-1}) = \text{tr}(\mathbf{F}_Q^{n-1}) = 0,$$

and the proof proceeds in a completely analogous manner.

By definition and assumption, we have

$$\begin{aligned}\mathrm{tr}(\mathbf{F}_{\mathbf{Q}}^n) &= \xi(\phi)\mathrm{tr}(\mathbf{Q}^n) = 0, \\ \mathrm{tr}(\mathbf{C}_{\mathbf{Q}}^n) &= -\mathrm{tr}(\mathbf{v} \cdot \nabla \mathbf{Q}^n) + \mathrm{tr}(\mathbf{S}^n) = -\mathbf{v} \cdot \nabla \mathrm{tr}(\mathbf{Q}^n) + \mathrm{tr}(\mathbf{S}^n) = \mathrm{tr}(\mathbf{S}^n), \\ \mathrm{tr}(\mathbf{G}_{\mathbf{Q}}^n) &= -\mathrm{tr}(\mathbf{H}^n).\end{aligned}$$

Therefore, it remains to show that

$$\mathrm{tr}(\mathbf{S}^n) = 0 \text{ and } \mathrm{tr}(\mathbf{H}^n) = 0.$$

A direct calculation yields

$$\begin{aligned}\mathrm{tr}(\mathbf{S}^n) &= [\mathrm{tr}(\boldsymbol{\Omega}^n \cdot \mathbf{Q}^n - \mathbf{Q}^n \cdot \boldsymbol{\Omega}^n)] + a[\mathrm{tr}(\mathbf{Q}^n \cdot \mathbf{D}^n + \mathbf{D}^n \cdot \mathbf{Q}^n)] + \frac{2a}{d}\mathrm{tr}(\mathbf{D}^n) - 2a[(\mathbf{D}^n : \mathbf{Q}^n)\mathrm{tr}(\mathbf{Q}^n + \frac{1}{d}\mathbf{I})] \\ &= [\mathrm{tr}(\boldsymbol{\Omega}^n \cdot \mathbf{Q}^n) - \mathrm{tr}(\mathbf{Q}^n \cdot \boldsymbol{\Omega}^n)] + a[\mathrm{tr}(\mathbf{Q}^n \cdot \mathbf{D}^n) + \mathrm{tr}(\mathbf{D}^n \cdot \mathbf{Q}^n)] - 2a(\mathbf{D}^n : \mathbf{Q}^n)\end{aligned}$$

where we have used  $\mathrm{tr}(\mathbf{D}^n) = \nabla \cdot \mathbf{v}^n = 0$  and  $\mathrm{tr}(\mathbf{Q}^n) = 0$ . Using the cyclic property of the trace and symmetry of  $\mathbf{D}^n$ , we obtain

$$\mathrm{tr}(\mathbf{S}^n) = 2a\mathrm{tr}(\mathbf{D}^n \cdot \mathbf{Q}^n) - 2a\mathrm{tr}((\mathbf{D}^n)^\top \cdot \mathbf{Q}^n) = 0.$$

Analogously, we have

$$\begin{aligned}\mathrm{tr}(\mathbf{H}^n) &= \mathrm{tr}(\nabla \cdot (K\nabla \mathbf{Q}^n)) - W\mathrm{tr}(\mathbf{Q}^n - \mathbf{Q}_*) - \kappa\mathrm{tr}(\mathbf{Q}^n - \mathbf{Q}^{n-1}) \\ &\quad - \mathrm{tr}\left[\alpha(\phi)\mathbf{Q}^n - \beta(\phi)\left((\mathbf{Q}^n)^2 - \frac{\mathrm{tr}((\mathbf{Q}^n)^2)}{d}\mathbf{I} + \gamma(\phi)\mathrm{tr}((\mathbf{Q}^n)^2)\mathrm{tr}(\mathbf{Q}^n)\right)\right] \\ &= \nabla \cdot (K\nabla \mathrm{tr}(\mathbf{Q}^n)) - W\mathrm{tr}(\mathbf{Q}^n) + W\mathrm{tr}(\mathbf{Q}_*) - \kappa\mathrm{tr}(\mathbf{Q}^n) + \kappa\mathrm{tr}(\mathbf{Q}^{n-1}) \\ &\quad - \alpha(\phi)\mathrm{tr}(\mathbf{Q}^n) + \beta(\phi)\mathrm{tr}\left((\mathbf{Q}^n)^2 - \frac{\mathrm{tr}((\mathbf{Q}^n)^2)}{d}\mathbf{I}\right) - \gamma(\phi)\mathrm{tr}((\mathbf{Q}^n)^2)\mathrm{tr}(\mathbf{Q}^n) = 0,\end{aligned}$$

where the last equality follows from the traceless property of  $\mathbf{Q}^n$  and  $\mathbf{Q}^{n-1}$ . Consequently,

$$\mathrm{tr}(B_k(\mathbf{C}_{\mathbf{Q}}^n)) = \mathrm{tr}(B_k(\mathbf{G}_{\mathbf{Q}}^n)) = \mathrm{tr}(B_k(\mathbf{F}_{\mathbf{Q}}^n)) = 0.$$

According to (3.6), we have

$$\mathrm{tr}(\mathbf{H}^{n+1}) = \begin{cases} \nabla \cdot (K\nabla \mathrm{tr}(\mathbf{Q}^{n+1})) - (W + \kappa)\mathrm{tr}(\mathbf{Q}^{n+1}), & \text{(SGE-BDF1)} \\ \nabla \cdot (K\nabla \mathrm{tr}(\mathbf{Q}^{n+1})) - \tau(W + \kappa)\alpha_2\mathrm{tr}(\mathbf{Q}^{n+1}), & \text{(SGE-BDF2)}. \end{cases} \quad (3.14)$$

Combining (3.12) and (3.14) yields a scalar Poisson problem for  $\mathrm{tr}(\mathbf{Q}^{n+1})$ . In the SGE-BDF1 case this takes the form

$$\left[\frac{\alpha_k}{\tau} + \kappa + W - \nabla \cdot (K\nabla(\bullet))\right]\mathrm{tr}(\mathbf{Q}^{n+1}) = 0. \quad (3.15)$$

with the proposed boundary conditions. The unique solution is thus  $\mathrm{tr}(\mathbf{Q}^{n+1}) = 0$ . An identical argument applies to SGE-BDF2. Hence  $\mathrm{tr}(\mathbf{Q}^{n+1}) = 0$  and the induction is complete.  $\square$

**Remark 3.3** We remark that the unique solvability of (3.15) relies on imposed boundary conditions. For example, in the case of the Dirichlet boundary condition, equation (3.15) reduces to a Poisson equation with homogeneous Dirichlet boundary data, which admits a unique solution.

For the homogeneous Neumann boundary condition imposed on  $\mathbf{Q}$ , equation (3.15) becomes a Poisson equation equipped with the homogeneous Neumann boundary condition. In this case, unique solvability is guaranteed in the sense

$$\int_{\Omega} \text{tr}(\mathbf{Q}^{n+1}) \, d\mathbf{x} = 0,$$

which fixes the additive constant and ensures uniqueness of the solution.

We now investigate energy stability of the algorithms. We first prove that the SGE-BDF1 scheme is energy stable with a sufficiently large stabilization parameter  $\kappa$ . This proof contains the main cancellation mechanism in the SGE reformulation. **The proof for the energy stability of the SGE-BDF2 algorithm involves several additional estimates for the extrapolated bulk molecular field. It is presented separately in Appendix A.**

The analyses rest upon an assumption on the pointwise boundedness of  $\mathbf{Q}^n$ :

$$\max_{n=1, \dots, N_t} \max_{\mathbf{x} \in \Omega} \|\mathbf{Q}^n\| \leq M, \quad (3.16)$$

where  $M > 0$  is a constant.

In our numerical solutions of the model, condition (3.16) holds whenever the numerical solution doesn't blow up. Physically, it should not as an order parameter tensor for liquid crystals. For the continuous active liquid crystal model with the polynomial bulk free energy density, a proof for the pointwise boundedness of  $\mathbf{Q}$  model is not available. As the result, a fully rigorous proof at the discrete level would require a comprehensive convergence analysis using the inductive arguments analogous to those in [40, 62], which is far beyond the scope of this study. Nevertheless, extensive computations confirm that the stabilization strategy delivers both robustness and efficiency in many scenarios and the boundedness of  $\mathbf{Q}^n$  is never an issue. [52–54, 56].

**Lemma 3.1** Under the hypothesis, (3.16), energy functional  $F_{\kappa}(\mathbf{Q})$  defined by

$$\begin{aligned} F_{\kappa}(\mathbf{Q}) &= \int_{\Omega} \frac{\kappa}{2} \text{tr}(\mathbf{Q}^2) - \left[ \frac{\alpha}{2} \text{tr}(\mathbf{Q}^2) - \frac{\beta}{3} \text{tr}(\mathbf{Q}^3) + \frac{\gamma}{4} \text{tr}(\mathbf{Q}^2)^2 \right] \, d\mathbf{x} \\ &= \frac{\kappa}{2} \|\mathbf{Q}\|^2 - F_{\text{bulk}}(\mathbf{Q}) \end{aligned} \quad (3.17)$$

is convex in  $\Omega$  for sufficiently large  $\kappa > 0$ .

*Proof.* To complete the proof, we only need to verify that the second-order variation of  $F_{\kappa}(\mathbf{Q})$  is non-negative. Indeed, for any  $\mathbf{P} \in \mathcal{M}_0$ , a direct calculation gives

$$D_2 F_{\kappa}(\mathbf{Q})[\mathbf{P}, \mathbf{P}] = \int_{\Omega} (\kappa - \alpha) \text{tr}(\mathbf{P}^2) + 2\beta \text{tr}(\mathbf{Q}\mathbf{P}^2) - \gamma [\text{tr}(\mathbf{Q}^2) \text{tr}(\mathbf{P}^2) + 2(\text{tr}(\mathbf{P}\mathbf{Q}))^2] \, d\mathbf{x}.$$

We note that  $\mathbf{P} \in \mathcal{M}_0$  and therefore admits the decomposition  $\mathbf{P} = \mathbf{W}^{\top} \Lambda \mathbf{W} = \lambda_i \mathbf{w}_i \mathbf{w}_i^{\top}$ , where  $\mathbf{w}_i$ ,  $i = 1, \dots, d$  are orthonormal eigenvectors. Using  $|\mathbf{Q}| \leq M$ , we find

$$\begin{aligned} \text{tr}(\mathbf{Q}\mathbf{P}^2) &= \text{tr}(\lambda_i^2 \mathbf{Q} \mathbf{w}_i \mathbf{w}_i^{\top}) = \lambda_i^2 \mathbf{w}_i^{\top} \mathbf{Q} \mathbf{w}_i \leq M \sum_{i=1}^d \lambda_i^2 = M \text{tr}(\mathbf{P}^2), \\ \text{tr}(\mathbf{Q}^2) \text{tr}(\mathbf{P}^2) &\leq M^2 \text{tr}(\mathbf{P}^2), \quad [\text{tr}(\mathbf{P}\mathbf{Q})]^2 \leq |\mathbf{P}|^2 |\mathbf{Q}|^2 \leq M^2 \text{tr}(\mathbf{P}^2). \end{aligned}$$

Consequently, the second variation satisfies

$$D_2 F_{\kappa}(\mathbf{Q})[\mathbf{P}, \mathbf{P}] \geq [(\kappa - \alpha) - 2|\beta|M - 3|\gamma|M^2] \int_{\Omega} \text{tr}(\mathbf{P}^2) \, d\mathbf{x}.$$

Hence, by choosing  $\kappa \geq \alpha + 2|\beta|M + 3|\gamma|M^2$ , the functional  $F_{\kappa}(\mathbf{Q})$  is convex.  $\square$

**Lemma 3.2** Assuming the stabilization parameter satisfies the requirement of Lemma 3.1, we then have the following inequality:

$$F_{\text{bulk}}(\mathbf{Q}^{n+1}) - F_{\text{bulk}}(\mathbf{Q}^n) \leq (\kappa(\mathbf{Q}^{n+1} - \mathbf{Q}^n) + f_{\text{bulk}}(\mathbf{Q}^n), \mathbf{Q}^{n+1} - \mathbf{Q}^n),$$

*Proof.* Using the identity

$$(\mathbf{Q}^{n+1}, \mathbf{Q}^{n+1} - \mathbf{Q}^n) = \frac{1}{2}\|\mathbf{Q}^{n+1}\|^2 - \frac{1}{2}\|\mathbf{Q}^n\|^2 + \frac{1}{2}\|\mathbf{Q}^{n+1} - \mathbf{Q}^n\|^2. \quad (3.18)$$

By Lemma 3.1 and Taylor expansion, there exists  $\tilde{\mathbf{Q}} = (1-s)\mathbf{Q}^n + s\mathbf{Q}^{n+1}$ , with  $s \in [0, 1]$ , such that

$$\begin{aligned} F_{\kappa}(\mathbf{Q}^{n+1}) - F_{\kappa}(\mathbf{Q}^n) &= (\kappa\mathbf{Q}^n - f_{\text{bulk}}(\mathbf{Q}^n), \mathbf{Q}^{n+1} - \mathbf{Q}^n) + D_2F_{\kappa}(\tilde{\mathbf{Q}})[\mathbf{Q}^{n+1} - \mathbf{Q}^n, \mathbf{Q}^{n+1} - \mathbf{Q}^n] \\ &\geq (\kappa\mathbf{Q}^n - f_{\text{bulk}}(\mathbf{Q}^n), \mathbf{Q}^{n+1} - \mathbf{Q}^n). \end{aligned} \quad (3.19)$$

Multiplying (3.18) by  $\kappa$  and (3.19) by  $-1$ , and summing the resulting equations, we have

$$\begin{aligned} \left[\frac{\kappa}{2}\|\mathbf{Q}^{n+1}\|^2 - F_{\kappa}(\mathbf{Q}^{n+1})\right] - \left[\frac{\kappa}{2}\|\mathbf{Q}^n\|^2 - F_{\kappa}(\mathbf{Q}^n)\right] + \frac{\kappa}{2}\|\mathbf{Q}^{n+1} - \mathbf{Q}^n\|^2 \\ \leq (\kappa(\mathbf{Q}^{n+1} - \mathbf{Q}^n) + f_{\text{bulk}}(\mathbf{Q}^n), \mathbf{Q}^{n+1} - \mathbf{Q}^n). \end{aligned} \quad (3.20)$$

Combining (3.20) and (3.17), we obtain the desired result.  $\square$

**Theorem 3.2** Provided that the stabilization parameter is sufficiently large so that the condition in Lemma 3.1 is satisfied, the total energy in the SGE-BDF1 scheme satisfies the following inequality

$$\begin{aligned} E_{\text{BDF1}}^{n+1} - E_{\text{BDF1}}^n &\leq -2\tau\|\sqrt{\eta}\mathbf{D}^{n+1}\|^2 - \tau\|\sqrt{b}\mathbf{v}^{n+1}\|^2 - \tau\|\sqrt{\Gamma_{\mathbf{Q}}}\mathbf{H}^{n+1}\|^2 \\ &\quad - \frac{\tau}{2}\|\mathbf{v}^{n+1} - \mathbf{v}^n\|^2 - \frac{\tau}{2}\|\sqrt{K}\nabla(\mathbf{Q}^{n+1} - \mathbf{Q}^n)\|^2 + \tau(\mathbf{Q}^n, \chi\mathbf{D}^{n+1} - \xi\mathbf{H}^{n+1}), \end{aligned}$$

where

$$E_{\text{BDF1}}^n = \int_{\Omega} \left[ \frac{1}{2}|\mathbf{v}^n|^2 + \frac{K}{2}|\nabla\mathbf{Q}^n|^2 + \frac{W}{2}|\mathbf{Q}^n - \mathbf{Q}^*|^2 \right] d\mathbf{x} + F_{\text{bulk}}(\mathbf{Q}^n).$$

So, the scheme is energy stable for passive liquid crystal systems.

*Proof.* Taking the inner products of the first and third equations of (3.5), respectively, with  $\mathbf{g}_{\mathbf{v}}^{n+1} = \mathbf{v}^{n+1}$  and  $\mathbf{G}_{\mathbf{Q}}^{n+1} = -\mathbf{H}_{\text{BDF1}}^{n+1}$ , integrating by parts, and using  $\nabla \cdot \mathbf{v}^{n+1} = 0$ , one obtains

$$\begin{aligned} \frac{1}{\tau}(\mathbf{v}^{n+1} - \mathbf{v}^n, \mathbf{v}^{n+1}) &= -2\|\sqrt{\eta}\mathbf{D}^{n+1}\|^2 - \|\sqrt{b}\mathbf{v}^{n+1}\|^2 + (\mathbf{f}_{\mathbf{v}}^n, \mathbf{v}^{n+1}), \\ &\quad + \zeta^{n+1}(\mathbf{g}_{\mathbf{v}}^{n+1}, \mathbf{c}_{\mathbf{v}}^n) - \omega^{n+1}(\mathbf{g}_{\mathbf{v}}^{n+1}, \mathbf{g}_{\mathbf{v}}^n), \end{aligned} \quad (3.21)$$

$$\begin{aligned} \frac{1}{\tau}(\mathbf{Q}^{n+1} - \mathbf{Q}^n, \mathbf{G}_{\mathbf{Q}}^{n+1}) &= -\|\sqrt{\Gamma_{\mathbf{Q}}}\mathbf{H}^{n+1}\|^2 - (\mathbf{F}_{\mathbf{Q}}^n, \mathbf{H}^{n+1}) \\ &\quad + \zeta^{n+1}(\mathbf{G}_{\mathbf{Q}}^{n+1}, \mathbf{C}_{\mathbf{Q}}^n) - \omega^{n+1}(\mathbf{G}_{\mathbf{Q}}^{n+1}, \mathbf{G}_{\mathbf{Q}}^n). \end{aligned} \quad (3.22)$$

A straightforward computation using Lemma 3.2 yields

$$(\mathbf{v}^{n+1} - \mathbf{v}^n, \mathbf{v}^{n+1}) = \frac{1}{2}\|\mathbf{v}^{n+1}\|^2 - \frac{1}{2}\|\mathbf{v}^n\|^2 + \frac{1}{2}\|\mathbf{v}^{n+1} - \mathbf{v}^n\|^2, \quad (3.23)$$

$$\begin{aligned}
(\mathbf{Q}^{n+1} - \mathbf{Q}^n, \mathbf{G}_Q^{n+1}) &= -(\mathbf{Q}^{n+1} - \mathbf{Q}^n, \nabla \cdot (K \nabla \mathbf{Q}^{n+1})) + W(\mathbf{Q}^{n+1} - \mathbf{Q}^*, \mathbf{Q}^{n+1} - \mathbf{Q}^n) \\
&\quad + (\mathbf{Q}^{n+1} - \mathbf{Q}^n, \kappa(\mathbf{Q}^{n+1} - \mathbf{Q}^n) + f_{\text{bulk}}(\mathbf{Q}^n)) \\
&\geq \frac{1}{2} \|\sqrt{K} \nabla \mathbf{Q}^{n+1}\|^2 - \frac{1}{2} \|\sqrt{K} \nabla \mathbf{Q}^n\|^2 + \frac{1}{2} \|\sqrt{K} \nabla (\mathbf{Q}^{n+1} - \mathbf{Q}^n)\|^2 \\
&\quad + \frac{1}{2} \|\sqrt{W}(\mathbf{Q}^{n+1} - \mathbf{Q}_*)\|^2 - \frac{1}{2} \|\sqrt{W}(\mathbf{Q}^n - \mathbf{Q}_*)\|^2 + \frac{1}{2} \|\sqrt{W}(\mathbf{Q}^{n+1} - \mathbf{Q}^n)\|^2 \\
&\quad + F_{\text{bulk}}(\mathbf{Q}^{n+1}) - F_{\text{bulk}}(\mathbf{Q}^n)
\end{aligned} \tag{3.24}$$

$$\begin{aligned}
\zeta^{n+1}(\mathbf{g}_v^{n+1}, \mathbf{c}_v^n) - \omega^{n+1}(\mathbf{g}_v^{n+1}, \mathbf{g}_v^n) + \zeta^{n+1}(\mathbf{G}_Q^{n+1}, \mathbf{C}_Q^n) - \omega^{n+1}(\mathbf{G}_Q^{n+1}, \mathbf{G}_Q^n) \\
= \mathcal{G}(\mathbf{g}_v^n, \mathbf{G}_Q^n) \zeta^{n+1} \omega^{n+1} - \mathcal{G}(\mathbf{g}_v^n, \mathbf{G}_Q^n) \omega^{n+1} \zeta^{n+1} = 0.
\end{aligned} \tag{3.25}$$

Summing (3.21) and (3.22) and substituting the identities (3.23)-(3.25), one directly arrives at the discrete energy inequality.  $\square$

**Remark 3.4** The condition on the stabilization parameter  $\kappa$  in Theorem 3.2 is a sufficient condition for ensuring energy stability of the algorithm at the theoretical level. Because stabilization methods are intrinsically connected to convex-splitting approaches, such conditions are commonly imposed to guarantee the convexity of the bulk free energy required in the analysis. They are, however, generally not necessary in practical computations.

In practice, the choice of  $\kappa$  must be balanced against the time-step size  $\tau$ . A smaller  $\kappa$  may lead to a loss of convexity in the bulk free energy and thereby induce possible energy growth, but this effect can often be compensated for by taking a sufficiently small  $\tau$ . Conversely, a larger  $\kappa$  enhances stability and permits larger time steps. However, choosing a large  $\kappa$  together with a large time-step size may perturb the discrete system substantially away from the continuum model, leading to considerable numerical error.

Thus, the interplay between  $\kappa$  and  $\tau$  is primarily a practical implementation issue, and these parameters should be calibrated with care. Figure 3 shows that energy stability can be achieved even when  $\kappa$  is below the theoretical bound, provided that  $\tau$  is chosen appropriately.

### 3.3. Second-order linearly implicit schemes based on the discrete gradient scheme

The SGE-BDF1 and SGE-BDF2 schemes are both robust and efficient; however, their energy stability proofs require a relatively large stabilization parameter. To address this limitation, we adopt the polarized discrete gradient (PDG) approach [42, 63]. In this method, a mild stabilization parameter  $\kappa$  would warrant energy stability **while compared with the SGE-BDF1 scheme**. The role of the stabilization parameter is to guarantee solvability of the  $\mathbf{Q}$ -tensor system. Specifically, it suffices to take  $\kappa \geq \max\{0, -\alpha\}$ . Unlike the previous schemes, no additional assumption on  $\kappa$  is required to establish energy stability. The resulting second-order SGE-PDG scheme is formulated as follows:

$$\begin{cases} \frac{\mathbf{v}^{n+1} - \mathbf{v}^{n-1}}{2\tau} = -\nabla p^{\bar{n}} + 2\nabla \cdot (\eta \mathbf{D}^{\bar{n}}) - b\mathbf{v}^{\bar{n}} + \bar{\zeta}^n \mathbf{c}_v^n - \bar{\omega}^n \mathbf{g}_v^n + \mathbf{f}_v^n, \\ \nabla \cdot \mathbf{v}^{\bar{n}} = 0, \\ \frac{\mathbf{Q}^{n+1} - \mathbf{Q}^{n-1}}{2\tau} = \Gamma_Q \bar{\mathbf{H}}^n + \bar{\zeta}^n \mathbf{C}_Q^n - \bar{\omega}^n \mathbf{G}_Q^n + \mathbf{F}_Q^n, \\ \bar{\zeta}^n = \frac{(\bar{\mathbf{g}}_v^n, \bar{\mathbf{g}}_v^n) + (\bar{\mathbf{G}}_Q^n, \bar{\mathbf{G}}_Q^n)}{\mathcal{G}(\bar{\mathbf{g}}_v^n, \bar{\mathbf{G}}_Q^n)}, \quad \bar{\omega}^n = \frac{(\bar{\mathbf{g}}_v^n, \mathbf{c}_v^n) + (\bar{\mathbf{G}}_Q^n, \mathbf{C}_Q^n)}{\mathcal{G}(\bar{\mathbf{g}}_v^n, \bar{\mathbf{G}}_Q^n)}, \end{cases} \tag{3.26}$$

where  $(\bullet)^{\bar{n}} = \frac{(\bullet)^{n+1} + (\bullet)^{n-1}}{2}$ ,

$$\bar{\mathbf{H}}^n = \nabla \cdot (K \nabla \mathbf{Q}^{\bar{n}}) - W(\mathbf{Q}^{\bar{n}} - \mathbf{Q}_*) - \kappa(\mathbf{Q}^{\bar{n}} - \mathbf{Q}^n) - 2\bar{f}_{\text{bulk}}(\mathbf{Q}^{n-1}, \mathbf{Q}^n, \mathbf{Q}^{n+1}). \tag{3.27}$$

Here,  $\bar{f}_{\text{bulk}}(\bullet, \bullet, \bullet)$  is the PDG associated with the polarized energy  $\bar{F}_{\text{bulk}}(\bullet, \bullet)$  of  $F_{\text{bulk}}(\bullet)$ . We call  $\bar{F}_{\text{bulk}}(\bullet, \bullet)$  a polarized functional of  $F_{\text{bulk}}$  if it satisfies

$$\bar{F}_{\text{bulk}}(\mathbf{U}, \mathbf{U}) = F_{\text{bulk}}(\mathbf{U}), \quad \bar{F}_{\text{bulk}}(\mathbf{U}, \mathbf{V}) = \bar{F}_{\text{bulk}}(\mathbf{V}, \mathbf{U}). \quad (3.28)$$

The first property ensures consistency of  $\bar{F}_{\text{bulk}}(\bullet, \bullet)$  with the original energy, while the second enforces symmetry and thus guarantees the second-order accuracy. We then say that  $\bar{f}_{\text{bulk}}(\bullet, \bullet, \bullet)$  is the polarized discrete gradient of  $\bar{F}_{\text{bulk}}$  if, for all  $\mathbf{U}, \mathbf{V}, \mathbf{W}$ ,

$$2\bar{f}_{\text{bulk}}(\mathbf{U}, \mathbf{U}, \mathbf{U}) = f_{\text{bulk}}(\mathbf{U}), \quad (\bar{f}_{\text{bulk}}(\mathbf{U}, \mathbf{V}, \mathbf{W}), \mathbf{W} - \mathbf{U}) = \bar{F}_{\text{bulk}}(\mathbf{V}, \mathbf{W}) - \bar{F}_{\text{bulk}}(\mathbf{U}, \mathbf{V}). \quad (3.29)$$

The key to the PDG method is the selection of an appropriate polarized energy functional. With a judicious choice, one obtains a linearly implicit scheme. Here, we define the polarization of the bulk energy as follows:

$$\bar{F}_{\text{bulk}}(\mathbf{U}, \mathbf{V}) = \int_{\Omega} \left[ \frac{\alpha}{2} \frac{\text{tr}(\mathbf{U}^2) + \text{tr}(\mathbf{V}^2)}{2} - \frac{\beta}{3} \text{tr}(\mathbf{U}\mathbf{V}\frac{\mathbf{U}+\mathbf{V}}{2}) + \frac{\gamma}{4} \text{tr}(\mathbf{U}^2)\text{tr}(\mathbf{V}^2) \right] d\mathbf{x}. \quad (3.30)$$

The polarized discrete gradient  $\bar{f}_{\mathcal{N}}$  in (3.27) to (3.30) is as follows

$$\begin{aligned} \bar{f}_{\text{bulk}}(\mathbf{U}, \mathbf{V}, \mathbf{W}) &= \frac{\alpha}{2} \frac{\mathbf{U}+\mathbf{W}}{2} - \frac{\beta}{6} \left[ (\mathbf{V}^2 + \mathbf{V}\frac{\mathbf{U}+\mathbf{W}}{2} + \frac{\mathbf{U}+\mathbf{W}}{2}\mathbf{V}) \right. \\ &\quad \left. - \frac{1}{3} \text{tr}(\mathbf{V}(\mathbf{U} + \mathbf{V} + \mathbf{W}))\mathbf{I} \right] + \frac{\gamma}{2} \text{tr}(\mathbf{V}^2) \frac{\mathbf{U}+\mathbf{W}}{2}. \end{aligned} \quad (3.31)$$

**Remark 3.5** In the scalar scenarios, one can define the PDG using the following Itoh-Abe formulation

$$\bar{f}(u, v, w) = \frac{F(v, w) - F(u, v)}{w - u}. \quad (3.32)$$

However, (3.32) cannot be extended directly to tensor variables, since  $\mathbf{U}, \mathbf{W}$  and energy differences live in noncommutative tensor spaces, so the division is undefined.

We next demonstrate that if  $\text{tr}(\mathbf{Q}^0) = 0$  and the solution  $\mathbf{Q}^1$  is solved from a chosen startup scheme that is also traceless, then the SGE-PDG scheme preserves  $\text{tr}(\mathbf{Q}^n) = 0$  at every future step.

**Theorem 3.3** Suppose the SGE-PDG algorithm is initialized with  $\text{tr}(\mathbf{Q}^0)$  and  $\text{tr}(\mathbf{Q}^1) = 0$  both traceless and  $\nabla \cdot \mathbf{v}^0, \nabla \cdot \mathbf{v}^1 = 0$  both divergence-free, and choose  $\kappa \geq \max\{0, -\alpha\}$ . Then every subsequent solution  $\{\mathbf{v}^n, \mathbf{Q}^n\}_{n=2}^{N_t}$  produced by (3.26) satisfies  $\nabla \cdot \mathbf{v}^n = 0, \text{tr}(\mathbf{Q}^n) = 0$ .

*Proof.* The divergence-free condition follows immediately from the second formulation (3.26) by a straightforward inductive argument. It remains to show that  $\mathbf{Q}^{n+1}$  is traceless. By hypothesis,  $\text{tr}(\mathbf{Q}^0) = \text{tr}(\mathbf{Q}^1) = 0$ . Assume  $\text{tr}(\mathbf{Q}^k) = 0$  for  $k = 2, \dots, n$ . Taking the trace of the third equation in (3.26) and using the inductive assumption, we obtain

$$\begin{aligned} \frac{\text{tr}(\mathbf{Q}^{n+1})}{2\tau} &= \Gamma_{\mathbf{Q}} \text{tr}(\bar{\mathbf{H}}^n) + \bar{\zeta}^n \text{tr}(\mathbf{C}_{\mathbf{Q}}^n) - \bar{\omega}^n \text{tr}(\mathbf{G}_{\mathbf{Q}}^n), \\ &= \Gamma_{\mathbf{Q}} \text{tr}(\bar{\mathbf{H}}^n) + \bar{\zeta}^n \text{tr}(\mathbf{S}^n) \end{aligned} \quad (3.33)$$

By  $\nabla \cdot \mathbf{v}^n = 0$  and the facts that  $\mathbf{Q}^n$  is symmetric while  $\mathbf{\Omega}^n$  is skew-symmetric, we have

$$\begin{aligned} \text{tr}(\mathbf{S}^n) &= \text{tr}(a(\mathbf{Q}^n \mathbf{D}^n + \mathbf{D}^n \mathbf{Q}^n)) - \frac{2a}{d} (\mathbf{Q}^n : \mathbf{D}^n) \text{tr}(\mathbf{I}) \\ &= 2a \text{tr}(\mathbf{Q}^n \mathbf{D}^n) - 2a \mathbf{Q}^n : \mathbf{D}^n = 0. \end{aligned}$$

By straightforward calculations, one finds

$$\text{tr}(\bar{\mathbf{H}}^n) = \frac{1}{2} \nabla \cdot (K \Delta \text{tr}(\mathbf{Q}^{n+1})) - \frac{W + \kappa + \alpha}{2} \text{tr}(\mathbf{Q}^{n+1}) - \frac{\gamma}{2} |\mathbf{Q}^n|^2 \text{tr}(\mathbf{Q}^{n+1}). \quad (3.34)$$

Combining (3.33) and (3.34), we end up with the scalar Poisson problem with respect to  $\text{tr}(\mathbf{Q}^{n+1})$ :

$$\left[\frac{1}{2}\left(\frac{1}{\tau} + W + \kappa + \alpha + \gamma|\mathbf{Q}^n|^2\right) - \nabla \cdot (K\nabla(\bullet))\right] \text{tr}(\mathbf{Q}^{n+1}) = 0.$$

Whenever  $\kappa \geq \max\{0, -\alpha\}$ , by imposing boundary conditions on  $\text{tr}(\mathbf{Q}^{n+1})$  that are compatible with those prescribed for  $\mathbf{Q}^{n+1}$  (see Remark 3.3) and by invoking the classical theory of elliptic equations, the above problem admits a unique solution, satisfying

$$\text{tr}(\mathbf{Q}^{n+1}) = 0.$$

The proof is thus completed.  $\square$

Finally, we show that SGE-PDG preserves the energy dissipation rate even in the active liquid crystal case.

**Theorem 3.4** The discrete energy dissipation rate of the SGE-PDG scheme is given by

$$E_{\text{PDG}}^{n+1} - E_{\text{PDG}}^n = -2\tau\|\sqrt{\eta}\mathbf{D}^{\bar{n}}\|^2 - \tau\|\sqrt{b}\mathbf{v}^{\bar{n}}\|^2 - \tau\|\sqrt{\Gamma_{\mathbf{Q}}}\bar{\mathbf{H}}^n\|^2 + \tau(\mathbf{Q}^n, \chi\mathbf{D}^{\bar{n}} - \xi\bar{\mathbf{H}}^n),$$

where

$$E_{\text{PDG}}^n = \int_{\Omega} \frac{1}{2} \frac{|\mathbf{v}^{n-1}|^2 + |\mathbf{v}^n|^2}{2} + \frac{K}{2} \frac{|\nabla\mathbf{Q}^{n-1}|^2 + |\nabla\mathbf{Q}^n|^2}{2} + \frac{W}{2} \frac{|\mathbf{Q}^{n-1} - \mathbf{Q}_*|^2 + |\mathbf{Q}^n - \mathbf{Q}_*|^2}{2} + \frac{\kappa}{4} |\mathbf{Q}^n - \mathbf{Q}^{n-1}|^2 dx + \bar{F}_{\text{bulk}}(\mathbf{Q}^{n-1}, \mathbf{Q}^n).$$

For passive liquid crystal systems, it implies the scheme is unconditional energy stable.

*Proof.* Taking the inner-product of the first equation in (3.26) with  $\mathbf{v}^{\bar{n}}$  and using incompressibility from the continuity equation immediately yields

$$\begin{aligned} & \frac{1}{4\tau} \|\mathbf{v}^{n+1}\|^2 - \frac{1}{4\tau} \|\mathbf{v}^{n-1}\|^2 \\ &= (p^{\bar{n}}, \nabla \cdot \mathbf{v}^{\bar{n}}) - 2(\eta\mathbf{D}^{\bar{n}}, \mathbf{v}^{\bar{n}}) - (b\mathbf{v}^{\bar{n}}, \mathbf{v}^{\bar{n}}) + \bar{\zeta}^n(\mathbf{c}_{\mathbf{v}}^n, \bar{\mathbf{g}}_{\mathbf{v}}^n) - \bar{\omega}^n(\mathbf{g}_{\mathbf{v}}^n, \bar{\mathbf{g}}_{\mathbf{v}}^n) + (\mathbf{Q}^n, \chi\nabla\mathbf{v}^{\bar{n}}) \\ &= -2\|\sqrt{\eta}\mathbf{D}^{\bar{n}}\|^2 - \|\sqrt{b}\mathbf{v}^{\bar{n}}\|^2 + \bar{\zeta}^n(\mathbf{c}_{\mathbf{v}}^n, \bar{\mathbf{g}}_{\mathbf{v}}^n) - \bar{\omega}^n(\mathbf{g}_{\mathbf{v}}^n, \bar{\mathbf{g}}_{\mathbf{v}}^n) + (\mathbf{Q}^n, \chi\mathbf{D}^{\bar{n}}). \end{aligned} \quad (3.35)$$

Taking the inner-product of the third equation in (3.26) with  $\bar{\mathbf{G}}_{\mathbf{Q}}^n = -\bar{\mathbf{H}}^n$  yields

$$-\frac{1}{2\tau}(\mathbf{Q}^{n+1} - \mathbf{Q}^{n-1}, \bar{\mathbf{H}}^n) = -\|\sqrt{\Gamma_{\mathbf{Q}}}\bar{\mathbf{H}}^n\|^2 + \bar{\zeta}^n(\mathbf{C}_{\mathbf{Q}}^n, \bar{\mathbf{G}}_{\mathbf{Q}}^n) - \bar{\omega}^n(\mathbf{G}_{\mathbf{Q}}^n, \bar{\mathbf{G}}_{\mathbf{Q}}^n) - (\mathbf{Q}^n, \xi\bar{\mathbf{H}}^n). \quad (3.36)$$

Substituting the definition of  $\bar{\mathbf{H}}^n$  (3.27) then leads to

$$\begin{aligned} & -\frac{1}{2}(\mathbf{Q}^{n+1} - \mathbf{Q}^{n-1}, \bar{\mathbf{H}}^n) - (\bar{f}_{\text{bulk}}(\mathbf{Q}^{n-1}, \mathbf{Q}^n, \mathbf{Q}^{n+1}), \mathbf{Q}^{n+1} - \mathbf{Q}^{n-1}) \\ &= -\frac{1}{2}(\mathbf{Q}^{n+1} - \mathbf{Q}^{n-1}, \nabla \cdot (K\nabla\mathbf{Q}^{\bar{n}}) - W(\mathbf{Q}^{\bar{n}} - \mathbf{Q}_*) - \kappa(\mathbf{Q}^{\bar{n}} - \mathbf{Q}^n)) \\ &= \frac{1}{2}(K\nabla\mathbf{Q}^{\bar{n}}, \nabla\mathbf{Q}^{n+1} - \nabla\mathbf{Q}^{n-1}) + \frac{\kappa}{2}(\mathbf{Q}^{\bar{n}} - \mathbf{Q}^n, \mathbf{Q}^{n+1} - \mathbf{Q}^{n-1}) \\ & \quad + \frac{1}{2}(W(\frac{\mathbf{Q}^{n+1} - \mathbf{Q}_*}{2} + \frac{\mathbf{Q}^{n-1} - \mathbf{Q}_*}{2}), (\mathbf{Q}^{n+1} - \mathbf{Q}_*) - (\mathbf{Q}^{n-1} - \mathbf{Q}_*)) \\ &= \int_{\Omega} \frac{K}{4} (|\nabla\mathbf{Q}^{n+1}|^2 - |\nabla\mathbf{Q}^{n-1}|^2) + \frac{\kappa}{4} |\mathbf{Q}^{n+1} - \mathbf{Q}^n|^2 - \frac{\kappa}{4} |\mathbf{Q}^n - \mathbf{Q}^{n-1}|^2 dx, \\ & \quad + \int_{\Omega} \frac{W}{4} (|\mathbf{Q}^{n+1} - \mathbf{Q}_*|^2 - |\mathbf{Q}^{n-1} - \mathbf{Q}_*|^2) dx. \end{aligned} \quad (3.37)$$

By the definition of the discrete gradient (3.29), we obtain

$$(\bar{f}_{\text{bulk}}(\mathbf{Q}^{n-1}, \mathbf{Q}^n, \mathbf{Q}^{n+1}), \mathbf{Q}^{n+1} - \mathbf{Q}^{n-1}) = \bar{F}_{\text{bulk}}(\mathbf{Q}^n, \mathbf{Q}^{n+1}) - \bar{F}_{\text{bulk}}(\mathbf{Q}^{n-1}, \mathbf{Q}^n). \quad (3.38)$$

Finally, combining (3.35)-(3.38) with the following identity, (3.39),

$$\begin{aligned} & \bar{\zeta}^n(\mathbf{c}_v^n, \bar{\mathbf{g}}_v^n) - \bar{\omega}^n(\mathbf{g}_v^n, \bar{\mathbf{g}}_v^n) + \bar{\zeta}^n(\mathbf{C}_Q^n, \bar{\mathbf{G}}_Q^n) - \bar{\omega}^n(\mathbf{G}_Q^n, \bar{\mathbf{G}}_Q^n) \\ & = \mathcal{G}(\mathbf{g}_v^n, \mathbf{G}_Q^n) \bar{\zeta}^n \bar{\omega}^n - \mathcal{G}(\mathbf{g}_v^n, \mathbf{G}_Q^n) \bar{\omega}^n \bar{\zeta}^n = 0, \end{aligned} \quad (3.39)$$

completes the proof.  $\square$

The equations resulted from the SGE-PDG scheme are solved as follows.

- **Generalized Stokes equations.** For  $i = 1, 2, 3$ , find  $\mathbf{v}_i$  by solving:

$$\begin{cases} \frac{1}{2}(\frac{1}{\tau} + b)\mathbf{v}_i^{n+1} - \nabla \cdot (\eta \mathbf{D}(\mathbf{v}_i^{n+1})) + \nabla p^{n+1} = \mathbf{f}_i, \\ \nabla \cdot \mathbf{v}_i^{n+1} = 0. \end{cases} \quad (3.40)$$

Here,

$$\begin{aligned} \mathbf{f}_1 &= \frac{1}{2}(\frac{1}{\tau} - b)\mathbf{v}^{n-1} + \nabla \cdot (\eta \mathbf{D}(\mathbf{v}^{n-1})) + \mathbf{f}_v^n, \\ \mathbf{f}_2 &= \mathbf{c}_v^n, \quad \mathbf{f}_3 = \mathbf{g}_v^n. \end{aligned}$$

- **Coupled tensor-valued Poisson equations.** For  $i = 1, 2, 3$ , find  $\mathbf{Q}_i$  from

$$\mathcal{L}(\mathbf{Q}^n)\mathbf{Q}^{n+1} = \mathbf{F}_i, \quad (3.41)$$

where, the linear operator  $\mathcal{L}$  is

$$\begin{aligned} \mathcal{L}(\mathbf{Q}^n)\mathbf{Q} &= \left( \frac{1}{2\tau} + \frac{\kappa+W}{2}\Gamma_Q - \frac{\alpha\Gamma_Q}{2} - \frac{\beta\Gamma_Q}{6}\mathbf{Q}^n + \frac{\beta\Gamma_Q}{2}\text{tr}((\mathbf{Q}^n)^2) - \frac{\Gamma_Q}{2}\nabla \cdot (K\nabla(\bullet)) \right) \mathbf{Q}, \\ & - \frac{\beta\Gamma_Q}{6}\mathbf{Q}\mathbf{Q}^n + \frac{\beta\Gamma_Q}{9}\text{tr}(\mathbf{Q}^n\mathbf{Q})\mathbf{I}, \end{aligned}$$

and

$$\begin{aligned} \mathbf{F}_1 &= \left( \frac{1}{2\tau} + \frac{\Gamma_Q}{2}\nabla \cdot (K\nabla(\bullet)) - \frac{\kappa+W}{2}\Gamma_Q - \frac{\Gamma_Q\alpha(\phi)}{2} + \frac{\Gamma_Q\beta(\phi)}{6}\mathbf{Q}^n - \frac{\Gamma_Q\beta(\phi)}{2}\text{tr}((\mathbf{Q}^n)^2) \right) \mathbf{Q}^{n-1} \\ & + \Gamma_Q W \mathbf{Q}_* + \kappa \Gamma_Q \mathbf{Q}^n + \left( \frac{\Gamma_Q\beta(\phi)}{3}\mathbf{Q}^n + \frac{\Gamma_Q\beta(\phi)}{6}\mathbf{Q}^{n-1} \right) \mathbf{Q}^n \\ & - \frac{\Gamma_Q\beta(\phi)}{9}\text{tr}((\mathbf{Q}^n)^2)\mathbf{I} - \frac{\Gamma_Q\beta(\phi)}{9}\text{tr}(\mathbf{Q}^n\mathbf{Q}^{n-1})\mathbf{I} + \mathbf{F}_v^n, \\ \mathbf{F}_2 &= \mathbf{C}_Q^n, \quad \mathbf{F}_3 = \mathbf{G}_Q^n. \end{aligned}$$

Using this algorithm, a coupled Poisson equation system needs to be solved, rather than three separate Poisson equations as in the previous SGE-BDF1 algorithm.

#### 4. Spatial discretization and implementation

The spatial discretization of the afore-developed semidiscrete schemes is performed using finite difference schemes on a staggered grid [64, 65]. To ensure that the fully discrete scheme preserves the energy dissipation properties stated in Theorems 3.2 and 3.4, it is essential that the spatial discretization preserves discrete summation-by-parts (SBP) identities (see [66]), such as

$$\begin{aligned} (\nabla_h \cdot \mathbf{v}_h, p_h)_h &= -(\mathbf{v}_h, \nabla p_h)_h, \\ (\nabla_h \cdot (\eta \mathbf{D}_h) \mathbf{v}_h, \mathbf{u}_h)_h &= -(\eta \mathbf{D}_h(\mathbf{v}_h), \mathbf{D}_h(\mathbf{u}_h))_h, \\ (\nabla_h \cdot (K \nabla_h \mathbf{Q}_h), \mathbf{P}_h)_h &= -(K \nabla_h \mathbf{Q}_h, \nabla_h \mathbf{P}_h)_h. \end{aligned} \quad (4.1)$$

Here,  $(\cdot, \cdot)_h$  denotes the discrete inner product. The discrete inner product may depend on the location of variables on the staggered grid, but for simplicity, we do not introduce multiple distinct inner-product notations. The operators  $\nabla_h$  and  $\nabla_h \cdot$  represent the discrete gradient and divergence operation, respectively, and  $p_h, \mathbf{v}_h, \mathbf{Q}_h$  are the discrete counterparts of the physical variables. Identities in (4.1) can be ensured by employing a mark-and-cell (MAC) schemes, which warrants Theorems 3.2 and 3.4 after spatial discretizations.

**Remark 4.1** In structure-preserving frameworks, achieving full energy dissipation at the discrete level also requires the preservation of fundamental structural properties [under boundary conditions \(2.2\) and \(2.3\)](#):

$$(\mathbf{v} \cdot \nabla \mathbf{v}, \mathbf{v}) = 0, \quad (4.2)$$

$$(\mathbf{v} \cdot \nabla \mathbf{Q}, f'(\mathbf{Q})) = (\mathbf{v}, \nabla f(\mathbf{Q})) = -(f(\mathbf{Q}), \nabla \cdot \mathbf{v}) = 0. \quad (4.3)$$

To maintain (4.2), a common approach is to rewrite  $\mathbf{v} \cdot \nabla \mathbf{v}$  as  $B(\mathbf{v}, \mathbf{v}) = \frac{1}{2}[\mathbf{v} \cdot \nabla \mathbf{v} + \nabla \cdot (\mathbf{v}\mathbf{v})]$ , which leverages the divergence free condition, and can be discretized to preserve (4.2) due to its skew-symmetry property.

However, (4.3) is generally not preserved after spatial discretization if  $f(\cdot)$  is non-quadratic. Consequently, fully discrete energy-dissipative schemes cannot be constructed in the classical framework, even though the semi-discrete dissipation may still be achieved (see [27, 51]).

In contrast, under the SGE framework, both  $\mathbf{v} \cdot \nabla \mathbf{v}$  and  $\mathbf{v} \cdot \nabla \mathbf{Q}$  are inherently skew-symmetrized with respect to the energy gradient, allowing (4.2) and (4.3) to hold naturally, regardless of the spatial discretization.

In the practical implementation, all resulting linear systems are solved using a multigrid method. For the generalized Stokes system, we employ the Vanka smoother [67]. For scalar Poisson equations, the classical Gauss-Seidel method is used as a smoother. For vector-valued Poisson equations, a block Gauss-Seidel smoother is adopted and an additional projection step is included in the smoother to enforce the traceless property of  $\mathbf{Q}$ .

## 5. Numerical results

### 5.1. Convergence test

We begin by evaluating the spatial and temporal convergence properties of the three proposed schemes. In the absence of an analytical solution, we employ the following functions as the solution of governing system of equations (2.23) with a forcing term,

$$\begin{cases} u = \cos(t^2)(-\cos(2\pi x) \sin(2\pi y) + \sin(2\pi y)), \\ v = \cos(t^2)(\sin(2\pi x) \cos(2\pi y) - \sin(2\pi x)), \\ p = \cos(t^2) \cos(2\pi x) \cos(2\pi y), \\ \mathbf{Q} = \cos(t^2) \cos(4\pi x) \cos(4\pi y) \begin{pmatrix} 0.5 & 0.15 & 0 \\ 0.15 & 0.25 & 0 \\ 0 & 0 & -0.75 \end{pmatrix}. \end{cases}$$

In this test, all simulations are conducted on the unit square,  $\Omega = (0, 1)^2$ , with  $\Gamma = 10$ ,  $K = 10^{-3}$  and all remaining parameters are set to unity. Zero Dirichlet boundary conditions are employed to the velocity field and zero Neumann boundary conditions are imposed to all the components of the  $\mathbf{Q}$ -tensor field. [In all numerical experiments, if there is no additional explanation, the stabilization parameter is set to  \$\kappa = 5\$  for the SGE-BDF1 and SGE-BDF2 schemes, and to  \$\kappa = 1\$  for the SGE-PDG scheme.](#) For the SGE-BDF1 scheme, a fixed spatial grid of  $h = \frac{1}{512}$  is employed such that the spatial error is negligible while the time step is refined; [For the SGE-BDF2](#)

and SGE-PDG schemes, the spatial and temporal discretizations are refined simultaneously in order to verify the second-order convergence of the scheme in both space and time. At the termination time  $T = 1$ , the following discrete errors of the velocity and  $\mathbf{Q}$ -tensor are computed, and convergence rates are extracted via the log-log regression. The discrete errors are calculated by

$$\text{Error}_{\mathbf{v}} = \left( \sum_{i=1}^{N_x} \sum_{j=1}^{N_y} \left| \mathbf{v}_{i,j}^{N_t} - \mathbf{v}(x_i, y_j, T) \right|^2 \right)^{1/2}, \quad \text{Error}_{\mathbf{Q}} = \left( \sum_{i=1}^{N_x} \sum_{j=1}^{N_y} \left| \mathbf{Q}_{i,j}^{N_t} - \mathbf{Q}(x_i, y_j, T) \right|^2 \right)^{1/2}.$$

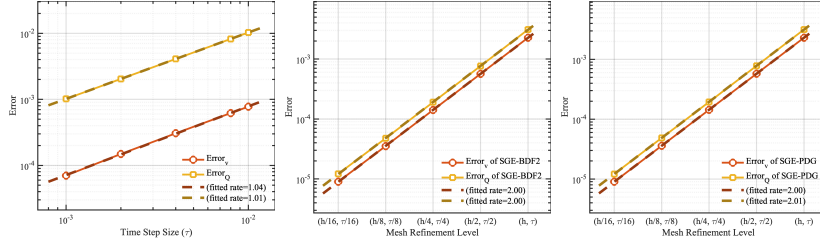


Figure 1: Mesh refinement test of the proposed schemes. The error is calculated at  $T = 1$ . Linear fitting is used to compute the convergence rate.

Figure 1 confirms first-order temporal convergence of the SGE-BDF1 scheme and second-order convergence in both spatial and temporal variables for the SGE-BDF2 and SGE-PDG schemes.

## 5.2. Interaction of a pair of $\pm \frac{1}{2}$ defects

In this example, we investigate the interaction of a pair of  $\pm \frac{1}{2}$  defects, and examine how their behavior is influenced by the presence of solid obstacles, the variation in activity parameters, and the effect of the boundary anchoring. The computational domain is defined as  $\Omega = (0, 1)^2$ . The initial condition is given by

$$\mathbf{Q}_0 = S_{eq} \left( \frac{\mathbf{n}_0 \mathbf{n}_0^\top}{\|\mathbf{n}_0\|^2} - \frac{\mathbf{I}}{3} \right), \quad \mathbf{n}_0 = (\cos \Theta, \sin \Theta, 0),$$

where

$$\Theta = \begin{cases} -0.5 \text{atan2}(y - 0.5, x - 0.3), & x < 0.5, \\ 0.5 \text{atan2}(y - 0.5, x - 0.7) + 3\pi, & \text{otherwise.} \end{cases}$$

The initial velocity is set to zero. Homogeneous Dirichlet boundary conditions are imposed on the velocity field, while homogeneous Neumann boundary conditions are applied to the  $\mathbf{Q}$ -tensor field at the boundary of the computational domain.

In this simulation, the obstacle is defined as an interior rectangle:  $D = (0.48, 0.52) \times (0.2, 0.8)$ . The model parameters are given as follows

$$b_{solid} = 10^5, \quad \eta_{fluid} = 1, \quad \eta_{solid} = 10^3, \quad K_{fluid} = 5 \times 10^{-4}, \\ N_{fluid} = 7.5, \quad N_{solid} = 0.1, \quad \Gamma_{fluid} = 10^2, \quad \Gamma_{solid} = 10^3, \quad A = \frac{2}{15}.$$

### 5.2.1. Results with the normal anchoring condition

We first compare the case without the rectangular obstacle with the case with the normal boundary anchoring at the obstacle.

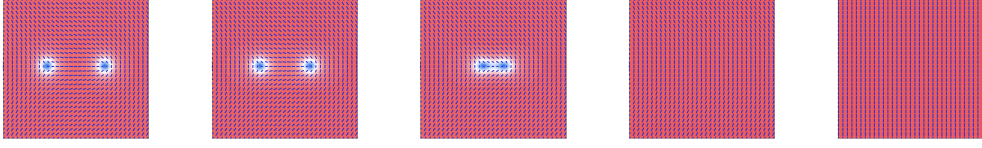


Figure 2: Interaction of a pair of passive  $\pm\frac{1}{2}$  defects without obstacles at times  $t = 0.1, 1, 2, 3, 20$ , respectively. The pair annihilate each other after a while.

Figure 2 shows the contour plots of the principal eigenvalue difference and the corresponding director field for a pair of passive  $\pm\frac{1}{2}$  defects at different time instances in the domain without any solid obstacles. Over time, the two defects gradually move toward each other due to their opposite topological charges. Eventually, they merge, leading to the complete annihilation of the defect pair. In the steady state, no defects remain in the system, indicating that the system has relaxed to a defect-free configuration. This result depicts the intrinsic energy-minimizing process of passive liquid crystals, in which oppositely charged defects attract and annihilate each other, ultimately yielding a uniform, topologically trivial state.

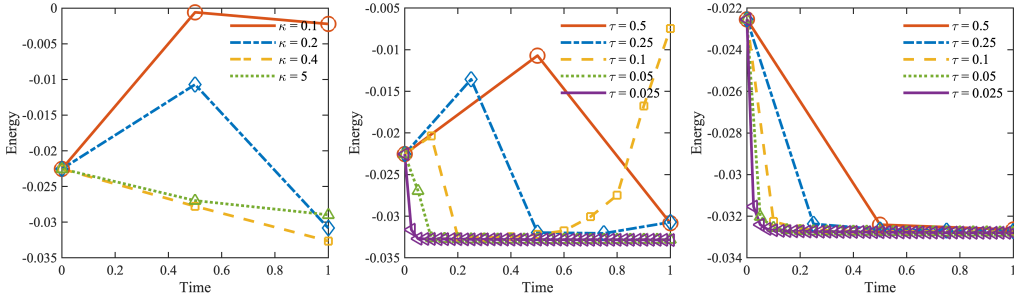


Figure 3: Free-energy evolution of the SGE-BDF1 scheme under several choices of the stabilization parameter,  $\kappa$ , and the time step size,  $\tau$ . Left: fixed  $\tau = 0.5$  with varying  $\kappa$ . Middle: fixed  $\kappa = 0.2$  with varying  $\tau$ . Right: fixed  $\kappa = 1$  with varying  $\tau$ . The results show that either a large stabilization parameter or a small time step,  $\tau$ , enforces monotone energy decay.

Figure 3 illustrates the interplay between the stabilization parameter,  $\kappa$ , and the time step size,  $\tau$ , in the SGE-BDF1 scheme. With  $\tau$  fixed (left), a large  $\kappa$  guarantees monotone energy decay. For smaller  $\kappa$ , this monotonicity may be lost.

However, as shown in the middle panel, reducing  $\tau$  can recover the expected energy dissipation even when  $\kappa$  is below the theoretical bound. In the right panel, for a relatively large  $\kappa$ , the scheme remains stable for all tested time steps.

These results indicate that the theoretical condition on  $\kappa$  is sufficient but not necessary in practice, and that a suitable balance between  $\kappa$  and  $\tau$  can ensure the energy stable behavior.

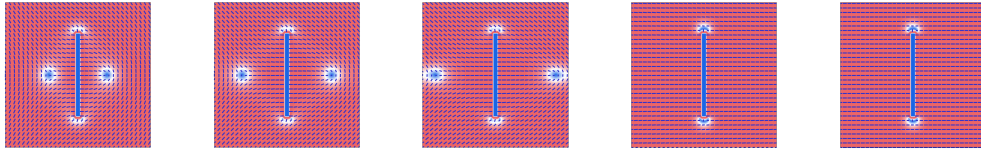


Figure 4: Interaction of a pair of passive  $\pm\frac{1}{2}$  defects with a rectangular obstacle under normal anchoring at times  $t = 0.1, 2, 3, 7.8, 20$ , respectively. The pair moves out of the computational domain after a while. The  $\mathbf{Q}$ -tensor is isotropic in the obstacle.

Figure 4 illustrates the dynamics of a pair of passive  $\pm\frac{1}{2}$  defects in a domain containing a rectangular obstacle positioned between them. Following a rapid initial relaxation, the orientation tensor field is zero within the solid at the time instances shown above, demonstrating the effectiveness of the proposed obstacle treatment.

In contrast to the case without obstacles, the two defects remain separated and symmetrically positioned with respect to the obstacle, which acts as a barrier due to its anchoring effect. Around  $t = 3$ , both defects exit the domain through the boundaries, resulting in a defect-free configuration. The final panel at  $t = 20$  confirms that the director field within the obstacle remains isotropic and stationary over long time evolution, further validating the effectiveness of the numerical approach.

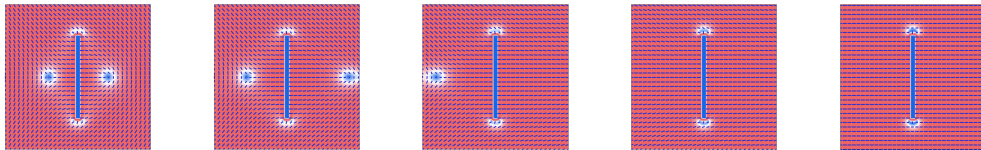


Figure 5: Interaction of a pair of active  $\pm\frac{1}{2}$  defects with a rectangular obstacle under normal anchoring at times  $t = 0.1, 1.8, 3.7, 5, 20$ , respectively, with parameter values  $\chi_{fluid} = 5$  and  $\xi_{fluid} = -0.1$ .

Figure 5 shows the dynamics of a pair of active  $\pm\frac{1}{2}$  defects in a domain containing a solid obstacle, with activity parameters (2.24) set at  $\chi_{fluid} = 5$  and  $\xi_{fluid} = -0.1$ . Similar to the passive case, the defects are repelled from each other due to anchoring effects imposed by both the obstacle and the domain boundary. However, a key difference arises from the presence of activity: the active  $+\frac{1}{2}$  defect moves more rapidly along its head direction compared to its passive counterpart, and therefore exits the domain earlier.

For the  $-\frac{1}{2}$  defect, the net effect of the active force is negligible, resulting in a slower departure. It gradually drifts away from the obstacle and eventually leaves the domain as well. The final panel at  $t = 20$  confirms that the director field within the obstacle remains isotropic and stationary over long time integration, consistent with earlier observations and validating the robustness of the numerical scheme.

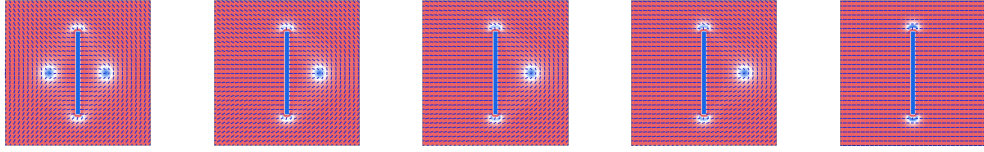


Figure 6: Interaction of a pair of active  $\pm\frac{1}{2}$  defects with a rectangular obstacle under normal anchoring at different times  $t = 0.1, 3, 5, 7, 20$ , respectively, with activity parameter values  $\chi_{fluid} = -5$  and  $\xi_{fluid} = 0.1$ . The left defect moves out of the computational domain sooner than the right one.

Figure 6 illustrates the dynamics of a pair of  $\pm\frac{1}{2}$  defects in a domain containing a solid obstacle, under activity parameter values  $\chi_{fluid} = -5$  and  $\xi_{fluid} = 0.1$ . The  $-\frac{1}{2}$  defect gradually drifts away from the obstacle and eventually exits the domain through the boundary. In contrast, the motion of the  $+\frac{1}{2}$  defect is strongly influenced by the negative activity parameter  $\chi_{fluid}$  and the anchoring condition. A negative activity parameter includes a force directed from head to tail, rather than in its usual head-forward direction. As a result, the  $+\frac{1}{2}$  defect moves more slowly than the  $-\frac{1}{2}$  in this scenario. The final panel at  $t = 20$  shows that both  $\pm\frac{1}{2}$  defects have exited the domain, and the director field remains isotropic and stationary within the solid region.

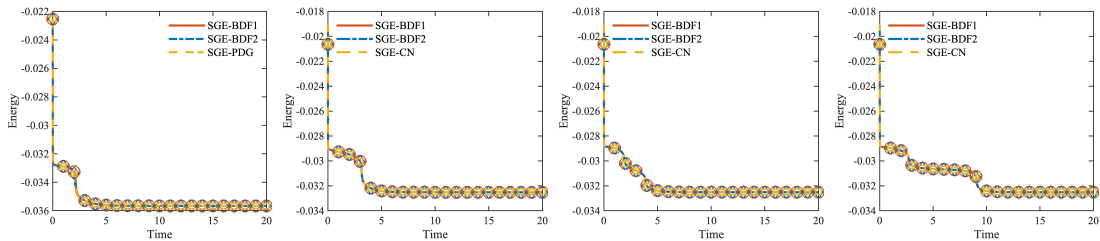


Figure 7: Time evolution of the free energy in the four different test cases with the solutions solved using the three proposed schemes. From left to right, the plots correspond to: (1) the passive liquid crystal without an obstacle; (2) the passive liquid crystal with a rectangular obstacle; (3) the active liquid crystal with  $\chi_{fluid} = 5$ ,  $\xi_{fluid} = -0.1$ ; and (4) the active liquid crystal with  $\chi_{fluid} = -5$ ,  $\xi_{fluid} = 0.1$ . In all cases, the energy decays in time.

Figure 7 presents the temporal evolution of the free energy in the four cases discussed above, computed using the three proposed numerical schemes. The energy profiles produced by the different schemes show excellent agreement, demonstrating the consistency and stability of the schemes.

For the passive liquid crystal cases, the free energy decays monotonically over time, as expected. In contrast, for active systems, the energy does not necessarily decrease monotonically due to the presence of active forcing. However, this non-monotonic behavior is less pronounced in the present example, as the activity parameters are relatively small. This phenomenon will be more clearly demonstrated in subsequent numerical experiments.

Notably, each energy curve exhibits one or more sudden drops, which correspond to events of the topological defects. These drops typically indicate that defect pairs have annihilated or exited the domain due to boundary anchoring. In the case with non-zero activity parameters, two distinct energy drops are observed, corresponding to the sequential disappearance of the  $+\frac{1}{2}$  and  $-\frac{1}{2}$  defects. In the other scenarios, only one energy drop is present, suggesting either simultaneous annihilation of the  $\pm\frac{1}{2}$  defects or simultaneous exits of the defects.

### 5.2.2. Solutions with different anchoring conditions

We compare the solutions of the model under different boundary anchoring conditions. In this section, the active parameters are set at  $\chi_{fluid} = -5$  and  $\xi_{fluid} = 0.1$ .

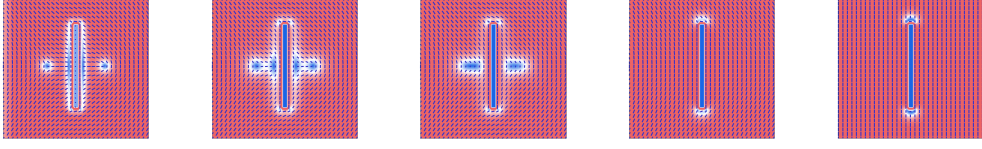


Figure 8: Interaction of a pair of active  $\pm \frac{1}{2}$  defects with a rectangular obstacle with the tangential anchoring at  $t = 0.01, 0.05, 0.1, 1.0, 20$ , respectively, with activity parameter values  $\chi_{fluid} = -5$  and  $\xi_{fluid} = 0.1$ . Defects disappear near the obstacle.

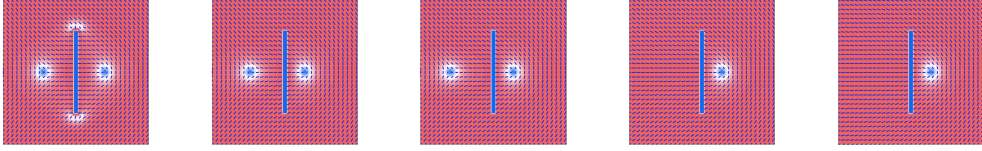


Figure 9: Interaction of a pair of active  $\pm \frac{1}{2}$  defects with a rectangular obstacle under anchoring consistent with the initial condition at  $t = 0.5, 3, 5, 7, 20$ , respectively, with activity parameter values  $\chi_{fluid} = -5$  and  $\xi_{fluid} = 0.1$ . The left defect leaves the computational domain after a while.

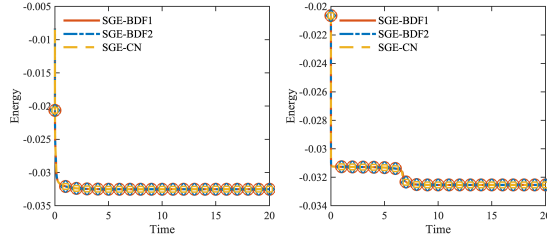


Figure 10: Time evolution of the free energy for two different test cases solved using the three proposed schemes. From the left to right, the plots correspond to: (1) the active liquid crystal with  $\chi_{fluid} = -5$  and  $\xi_{fluid} = 0.1$  with the tangential anchoring; and (2) the active liquid crystal with  $\chi_{fluid} = -5$  and  $\xi_{fluid} = 0.1$  with the anchoring consistent with the initial condition.

Figure 8 depicts the time evolution of the principal eigenvalue difference and the defect field for an active liquid crystal with weak tangential anchoring at the solid boundary. The defect is absorbed by the boundary due to the anchoring effect, and the system eventually reaches a steady state. Compared with the case of normal anchoring—where the steady-state defect field is aligned horizontally—here the director field is aligned vertically, reflecting the influence of the tangential anchoring at the solid boundary.

Figure 9 depicts the time evolution of the principal eigenvalue difference and the defect field

for the active liquid crystal under the anchoring condition

$$\mathbf{Q}|_{\partial D} = \mathbf{Q}_0|_{\partial D}.$$

The steady-state behavior differs from the previous cases. The  $-\frac{1}{2}$  defect gradually drifts away from the obstacle and eventually leaves the domain. In contrast, due to the active force and the imposed anchoring, the  $+\frac{1}{2}$  defect is driven from head to tail, causing it to move toward the obstacle where it is ultimately trapped. The final panel at  $t = 20$  shows that  $+\frac{1}{2}$  remains trapped in the domain in this scenario. Moreover, despite the continuous accumulation of active stress near the obstacle, the director field remains isotropic and stationary within the solid region, further validating the effectiveness of the proposed treatment for obstacles in long-time simulations.

Figures 10 show the corresponding free energy for the two cases. The energy curves obtained by the three different schemes are in close agreement; they decrease monotonically. These two cases illustrate the strong influence that the boundary anchoring can have on the defect dynamics.

### 5.3. Shape effect of the obstacle on the dynamics of active liquid crystals

In this example, we further investigate how the shape of the solid obstacle influences the dynamics of active liquid crystals. The computational domain is chosen as  $\Omega = (0, 4)^2$ . **Stabilization parameter is set to  $\kappa = 5$  in all cases.** The initial velocity field is set to zero, and the initial condition for the  $\mathbf{Q}$ -tensor field is defined as

$$\mathbf{Q}_0 = S_{eq} \left( \frac{\mathbf{n}_0 \mathbf{n}_0^\top}{\|\mathbf{n}_0\|^2} - \frac{\mathbf{I}}{3} \right), \quad \mathbf{n}_0 = \begin{cases} (1, 0, 0)^\top, & \sqrt{(x-2)^2 + (y-2)^2} < 0.5, \\ (0, 1, 0)^\top, & \text{otherwise.} \end{cases}$$

Homogeneous Dirichlet boundary conditions are imposed on the velocity field, while homogeneous Neumann boundary conditions are applied to the  $\mathbf{Q}$ -tensor field at the boundary of the computational domain. The model parameters are specified as follows

$$\begin{aligned} b_{solid} &= 10^5, \quad \eta_{fluid} = 1, \quad \eta_{solid} = 10^3, \quad K_{fluid} = 10^{-3}, \\ N_{fluid} &= 7.5, \quad N_{solid} = 0.1, \quad \Gamma_{fluid} = 10^2, \quad \Gamma_{solid} = 10^3, \quad A = \frac{2}{15}. \end{aligned}$$

We choose spatial step size as  $h = \frac{1}{64}$  and time step size as  $\tau = 5 \times 10^{-4}$ . In all the subsequent examples,  $\mathbf{Q}_*$  is chosen to be consistent with the initial condition,  $\mathbf{Q}_* = \mathbf{Q}_0$ .

We examine the evolution of active liquid crystals confined within solid obstacles of various shapes, under different signs of activity parameters. The following obstacle geometries are considered, each represented via indicator functions.

- Circle:

$$\phi = \begin{cases} 1, & \sqrt{(x-2)^2 + (y-2)^2} < 1.4, \\ 0, & \text{otherwise.} \end{cases}$$

- Horizontal ellipse:

$$\phi = \begin{cases} 1, & \left(\frac{x-2}{1.4}\right)^2 + \left(\frac{y-2}{0.7}\right)^2 < 1, \\ 0, & \text{otherwise.} \end{cases}$$

- Vertical ellipse:

$$\phi = \begin{cases} 1, & \left(\frac{x-2}{0.7}\right)^2 + \left(\frac{y-2}{1.4}\right)^2 < 1, \\ 0, & \text{otherwise.} \end{cases}$$

- Star:

$$\phi = \begin{cases} 1, & \sqrt{(x-2)^2 + (y-2)^2} < 1 + 0.4 \cos\left(5 \operatorname{atan2}(y-2, x-2)\right), \\ 0, & \text{otherwise.} \end{cases}$$

Figures 11–14 show the contour plots of the principal eigenvalue and the corresponding director field at selected time instances. In all cases, the initially circular defect splits into four distinct defects—two of type  $+\frac{1}{2}$  and two of type  $-\frac{1}{2}$ . These defects subsequently interact under the combined influence of boundary anchoring, active stresses, and mutual defect interactions.

A primary observation is that the post-splitting behavior strongly depends on the sign of the active parameter  $\chi_{fluid}$ . For  $\chi_{fluid} > 0$ , the initial circular defect splits into four defects, with two  $-\frac{1}{2}$  defects aligned vertically and two  $+\frac{1}{2}$  defects aligned horizontally. Whereas when  $\chi_{fluid} < 0$ , the alignment is reversed: the two  $-\frac{1}{2}$  defects appear horizontally, while the two  $+\frac{1}{2}$  defects are oriented vertically.

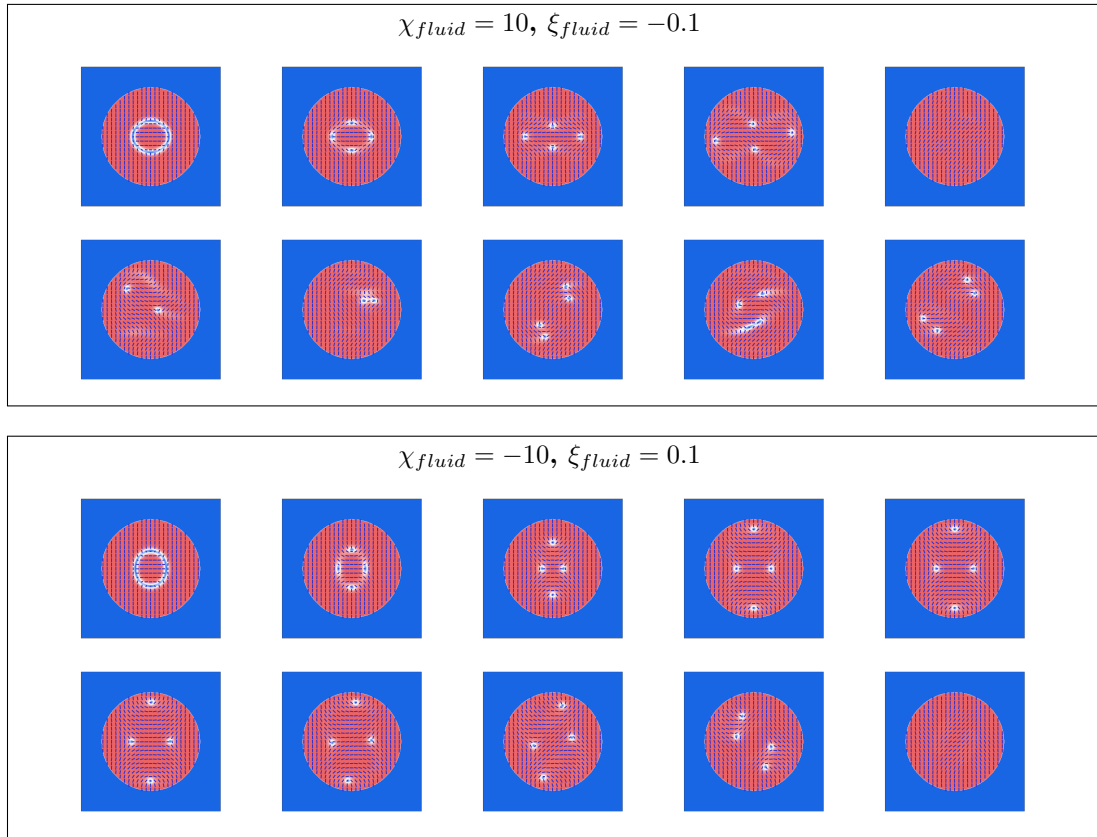


Figure 11: Comparison of defect dynamics for active liquid crystals with opposite signs of the activity in a circular domain. Each panel shows the contour of the principal eigenvalue and director field at various times. Both panels record the solutions at  $t = 0.1, 0.2, 0.5, 5, 7, 10, 13, 15, 17, 20$ , respectively.

The dynamics of defects exhibit notable differences depending on the shape of the obstacle. In the circular obstacle case, the two  $+\frac{1}{2}$  defects initially move apart due to active forces. Subsequently, their motion becomes irregular as a result of interactions among defects, boundary

anchoring, and strong active stresses. Due to high activities, the system does not approach a steady state in this scenario. As a result, we see dynamic defects form and go.

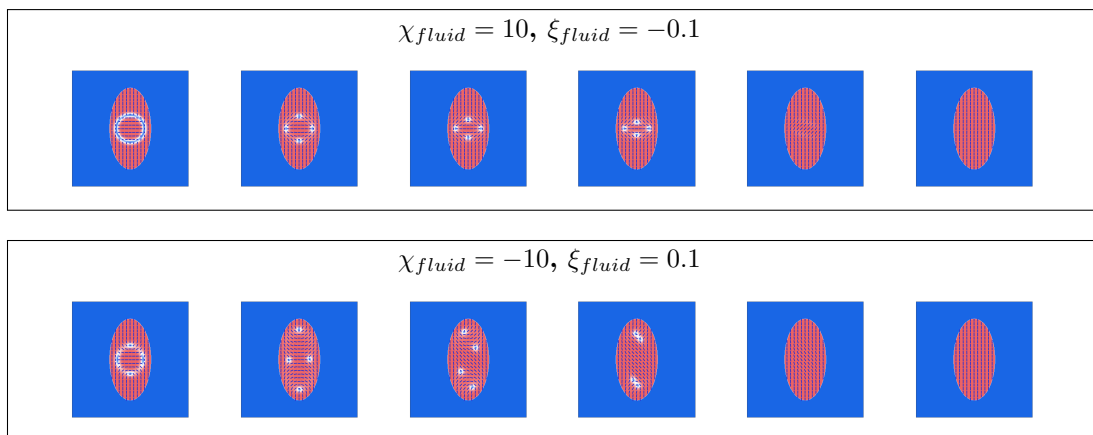


Figure 12: Comparison of defect dynamics for active liquid crystals with opposite signs of the activity in a vertical, elliptical domain. Each panel shows the contour of the principal eigenvalue and director field at various times. The top panel records the solutions at  $t = 0.1, 0.3, 1, 3, 5, 10$ , the bottom panel shows the solution at  $t = 0.2, 7, 10, 11, 12, 20$ , respectively.

In the vertically oriented elliptical obstacle, when  $\chi_{fluid} > 0$ , the two  $+\frac{1}{2}$  defects cannot separate significantly because of the geometric confinement. Eventually, the mutual attraction between the four defects leads them to merge and annihilate, eliminating all defects and driving the system toward a defect-free steady state.

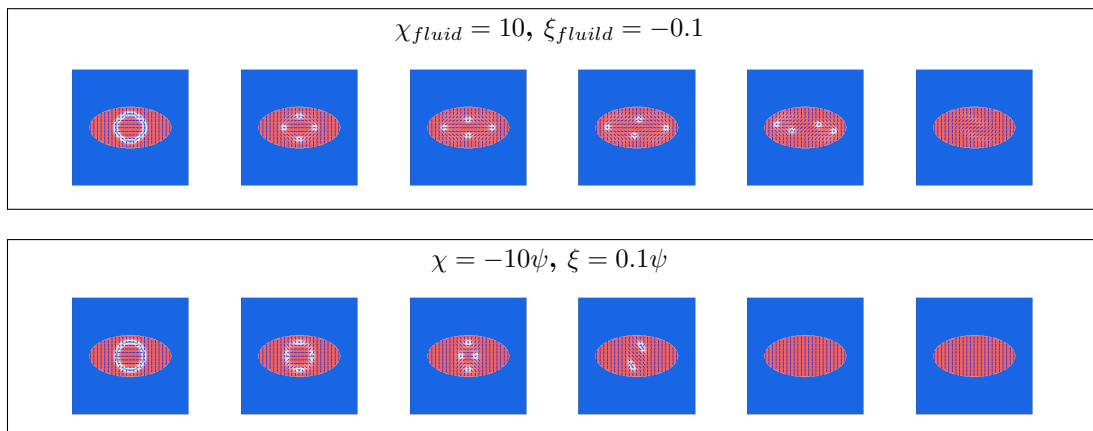


Figure 13: Comparison of defect dynamics for active liquid crystals with opposite signs of the activity in a horizontal, elliptical domain. Each panel shows the contour of the principal eigenvalue and director field at various time times. The top panel records the solutions at  $t = 0.1, 0.3, 1, 5, 7, 10$ , the bottom panel shows the solution at  $t = 0.1, 0.2, 5, 7.6, 10, 12$ , respectively.

For the horizontally oriented elliptical obstacle, when  $\chi_{fluid} > 0$ , the  $+\frac{1}{2}$  defects again initially move apart due to the active forcing, after which defect pairs annihilate and the system attains a steady state. For  $\chi_{fluid} < 0$ , a similar defect annihilation scenario occurs, but the motion of the  $+\frac{1}{2}$  defects is impeded by the solid boundary, leading to the rapid stabilization.

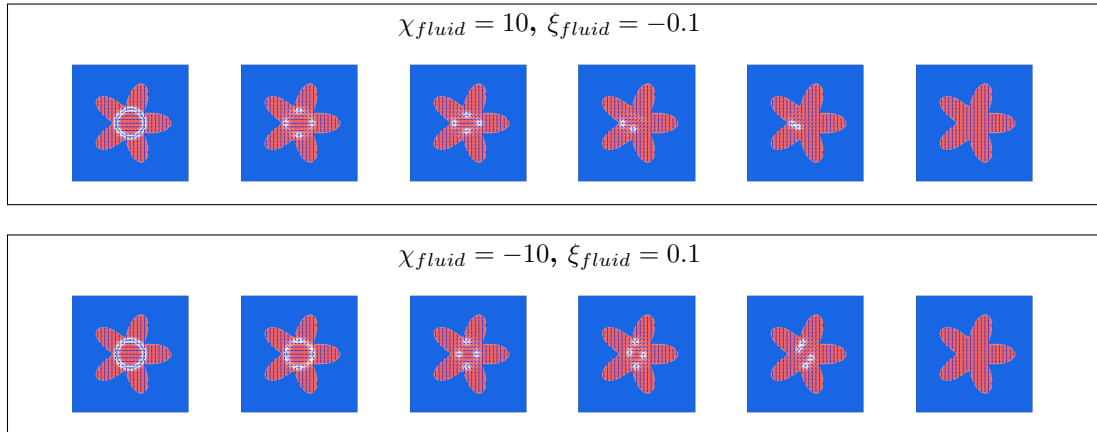


Figure 14: Comparison of defect dynamics for active liquid crystals with opposite signs of the activity in a star-shaped domain. Each panel shows the contour of the principal eigenvalue and director field at various time times. The top panel records the solutions at  $t = 0.1, 0.3, 1, 3, 3.5, 20$  the bottom panel shows the solution at  $t = 0.1, 0.2, 1, 3, 3.5, 20$ , respectively.

Finally, in the star-shaped domain, the dynamics resemble the horizontal ellipse case, rapidly approaching equilibrium.

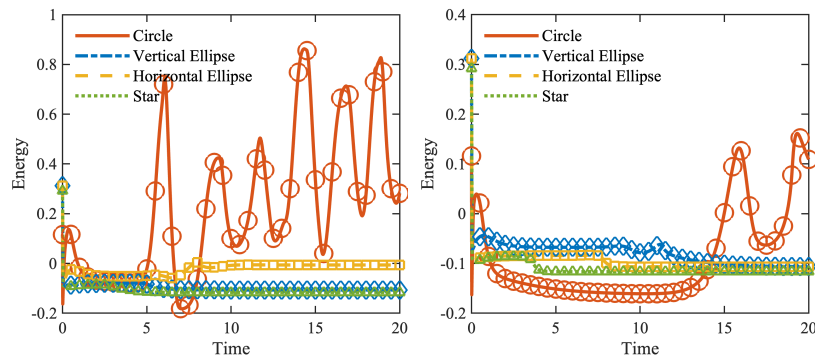


Figure 15: Temporal evolution of the free energy for active liquid crystals in domains with different obstacle shapes. The left panel corresponds to the case with  $\chi_{fluid} = 10$  and  $\xi_{fluid} = -0.1$ , while the right panel shows the results for  $\chi_{fluid} = -10$  and  $\xi_{fluid} = 0.1$ .

Figure 15 depicts the time evolution of the free energy for the aforementioned four cases, the left panel shows the result of  $\chi_{fluid} > 0$  and the right panel depicts the result of  $\chi_{fluid} < 0$ . One observes that in this case, due to large active parameter values, the energy is clearly no longer monotonically decreasing, especially in the case of the circular obstacle. Due to the geometric domain left for the defects to move around, their motion is primarily driven by the active stress. As a result, the system does not reach a steady state at the end of the computation. For other cases, they ultimately arrives at a steady state due to the effect between  $+\frac{1}{2}$  and  $-\frac{1}{2}$  defects and the confined geometry.

## 6. Conclusion

In this study, we have developed a set of thermodynamically consistent numerical algorithms for a novel  $\mathbf{Q}$ -tensor-based two-phase hydrodynamic model of active nematic liquid crystals and a solid substrate in a region of arbitrary geometry. The discrete equation system resulted from each algorithm consists of linear, decoupled solvers for the Stokes and Poisson systems, ensuring computational efficiency. Convergence tests confirm their first- and second-order temporal accuracy, respectively. For the passive model, the SGE-BDF2 scheme is shown in Appendix [Appendix A](#) to dissipate a modified energy under the boundedness and stabilization assumptions stated in the analysis, while the SGE-PDG scheme retains an unconditional second-order energy stability property. Through extensive numerical studies, we demonstrated how activity parameters and obstacle geometries influence defect dynamics and steady-state configurations. The proposed model and algorithms not only provide deeper physical insights into the hydrodynamics of the active nematic system but also establish a robust computational framework for future research in active matter. In particular, they furnish an efficient suite of tools to simulate two-phase active liquid crystals in domains with arbitrary solid boundaries or embedded obstacles of general shapes.

## Acknowledgements

Xuelong Gu's research is supported by NSF award OIA-2242812. and Qi Wang's research is partially supported by NSF awards OIA-2242812 and DMS-2038080, DOE award DE-SC0025229, and an SC GAIN-CRP award.

## Appendix A. Energy stability of the SGE–BDF2 scheme

This appendix provides the energy stability proof for the SGE–BDF2 scheme in the limit of passive liquid crystals. For any sequence  $f^n$ , we write

$$d_t f^{n+1} = f^{n+1} - f^n, \quad d_{2t} f^{n+1} = 3f^{n+1} - 4f^n + f^{n-1}, \quad d_{tt} f^n = f^{n+1} - 2f^n + f^{n-1},$$

and

$$D_t f^{n+1} = \frac{1}{\tau} d_t f^{n+1}, \quad D_{2t} f^{n+1} = \frac{1}{2\tau} d_{2t} f^{n+1}, \quad D_{tt} f^n = \frac{1}{\tau^2} d_{tt} f^n.$$

We assume that (3.16) holds. Consequently, for any  $\mathbf{A}$  and  $\mathbf{B}$  satisfying (3.16), there exists  $L_f > 0$  such that

$$\|f_{\text{bulk}}(\mathbf{A}) - f_{\text{bulk}}(\mathbf{B})\| \leq L_f \|\mathbf{A} - \mathbf{B}\|.$$

The BDF2 molecular field is given by

$$\mathbf{G}_{\mathbf{Q}}^{n+1} = -\nabla \cdot (K \nabla \mathbf{Q}^{n+1}) + W(\mathbf{Q}^{n+1} - \mathbf{Q}_*) + \frac{\tau \kappa}{2} d_{2t} \mathbf{Q}^{n+1} + B_2(f_N(\mathbf{Q}^n)).$$

**Lemma Appendix A.1** The following BDF2 identities hold:

$$2(d_{2t} f^{n+1}, f^{n+1}) = \|f^{n+1}\|^2 + \|B_2(f^{n+1})\|^2 - \|f^n\|^2 - \|B_2(f^n)\|^2 + \|d_{tt} f^n\|^2, \quad (\text{A.1})$$

$$\|d_{2t} f^{n+1}\|^2 = 6\|d_t f^{n+1}\|^2 - 2\|d_t f^n\|^2 + 3\|d_{tt} f^n\|^2. \quad (\text{A.2})$$

**Lemma Appendix A.2** For the BDF2 extrapolated nonlinear force, one has

$$d_{2t} F_{\text{bulk}}(\mathbf{Q}^{n+1}) \leq (d_{2t} \mathbf{Q}^{n+1}, B_2(f_{\text{bulk}}(\mathbf{Q}^n))) + 3L_f \|d_t \mathbf{Q}^{n+1}\|^2 + 3L_f \|d_t \mathbf{Q}^n\|^2. \quad (\text{A.3})$$

*Proof.* A direct calculation gives

$$\begin{aligned}
& (d_{2t}\mathbf{Q}^{n+1}, B_2(f_{\text{bulk}}(\mathbf{Q}^n))) \\
&= (3d_t\mathbf{Q}^{n+1} - d_t\mathbf{Q}^n, f_{\text{bulk}}(\mathbf{Q}^n) + d_t f_{\text{bulk}}(\mathbf{Q}^n)) \\
&= 3(d_t\mathbf{Q}^{n+1}, f_{\text{bulk}}(\mathbf{Q}^n)) + 3(d_t\mathbf{Q}^{n+1}, d_t f_{\text{bulk}}(\mathbf{Q}^n)) \\
&\quad - (d_t\mathbf{Q}^n, f_{\text{bulk}}(\mathbf{Q}^n)) - (d_t\mathbf{Q}^n, d_t f_{\text{bulk}}(\mathbf{Q}^n)).
\end{aligned}$$

The Taylor's formula with an integral remainder yields

$$\begin{aligned}
d_t F_{\text{bulk}}(\mathbf{Q}^{n+1}) &= (f_{\text{bulk}}(\mathbf{Q}^n), d_t\mathbf{Q}^{n+1}) \\
&\quad + \int_0^1 (1-s) (f'_{\text{bulk}}(\mathbf{Q}^n + sd_t\mathbf{Q}^{n+1})d_t\mathbf{Q}^{n+1}, d_t\mathbf{Q}^{n+1}) ds.
\end{aligned}$$

Therefore,

$$(f_{\text{bulk}}(\mathbf{Q}^n), d_t\mathbf{Q}^{n+1}) \geq d_t F_{\text{bulk}}(\mathbf{Q}^{n+1}) - \frac{L_f}{2} \|d_t\mathbf{Q}^{n+1}\|^2.$$

Similarly,

$$\begin{aligned}
d_t F_{\text{bulk}}(\mathbf{Q}^n) &= (d_t\mathbf{Q}^n, f_{\text{bulk}}(\mathbf{Q}^n)) \\
&\quad - \int_0^1 s (f'_{\text{bulk}}(\mathbf{Q}^n - sd_t\mathbf{Q}^n)d_t\mathbf{Q}^n, d_t\mathbf{Q}^n) ds,
\end{aligned}$$

hence

$$-(f_{\text{bulk}}(\mathbf{Q}^n), d_t\mathbf{Q}^n) \geq -d_t F_{\text{bulk}}(\mathbf{Q}^n) - \frac{L_f}{2} \|d_t\mathbf{Q}^n\|^2.$$

Moreover,

$$\|d_t f_{\text{bulk}}(\mathbf{Q}^n)\| \leq L_f \|d_t\mathbf{Q}^n\|.$$

It follows that

$$\begin{aligned}
3(d_t\mathbf{Q}^{n+1}, d_t f_{\text{bulk}}(\mathbf{Q}^n)) &\geq -3L_f \|d_t\mathbf{Q}^{n+1}\| \|d_t\mathbf{Q}^n\|, \\
-(d_t\mathbf{Q}^n, d_t f_{\text{bulk}}(\mathbf{Q}^n)) &\geq -L_f \|d_t\mathbf{Q}^n\|^2.
\end{aligned}$$

Combining the preceding estimates, we have

$$\begin{aligned}
& (d_{2t}\mathbf{Q}^{n+1}, B_2(f_{\text{bulk}}(\mathbf{Q}^n))) \\
&\geq d_{2t} F_{\text{bulk}}(\mathbf{Q}^{n+1}) - \frac{3L_f}{2} \|d_t\mathbf{Q}^{n+1}\|^2 - 3L_f \|d_t\mathbf{Q}^{n+1}\| \|d_t\mathbf{Q}^n\| - \frac{3L_f}{2} \|d_t\mathbf{Q}^n\|^2.
\end{aligned}$$

Since

$$2\|d_t\mathbf{Q}^{n+1}\| \|d_t\mathbf{Q}^n\| \leq \|d_t\mathbf{Q}^{n+1}\|^2 + \|d_t\mathbf{Q}^n\|^2,$$

the estimate (A.3) follows.  $\square$

**Theorem Appendix A.1** Let

$$\bar{\Gamma} = \|\Gamma_{\mathbf{Q}}\|_{L^\infty(\Omega)}, \quad \Theta = \frac{1}{2} \sqrt{\frac{\kappa}{\bar{\Gamma}}}.$$

Assume that

$$\kappa \geq \frac{9}{4} \bar{\Gamma} L_f^2. \tag{A.4}$$

Define the BDF2 energy by

$$\begin{aligned}
E_{\text{BDF2}}^{n+1} &= \frac{1}{4} (\|\mathbf{v}^{n+1}\|^2 + \|B_2(\mathbf{v}^{n+1})\|^2) \\
&+ \frac{1}{4} (\|\sqrt{K}\nabla\mathbf{Q}^{n+1}\|^2 + \|\sqrt{K}\nabla B_2(\mathbf{Q}^{n+1})\|^2) \\
&+ \frac{1}{4} (\|\sqrt{W}(\mathbf{Q}^{n+1} - \mathbf{Q}_*)\|^2 + \|\sqrt{W}B_2(\mathbf{Q}^{n+1} - \mathbf{Q}_*)\|^2) \\
&+ \frac{3}{2}F_{\text{bulk}}(\mathbf{Q}^{n+1}) - \frac{1}{2}F_{\text{bulk}}(\mathbf{Q}^n) + \left(2\Theta + \frac{3L_f}{2}\right) \|d_t\mathbf{Q}^{n+1}\|^2.
\end{aligned} \tag{A.5}$$

Then the SGE–BDF2 scheme in the limit of passive liquid crystals satisfies

$$\begin{aligned}
E_{\text{BDF2}}^{n+1} - E_{\text{BDF2}}^n + (4\Theta - 3L_f)\|d_t\mathbf{Q}^{n+1}\|^2 + \tau \left(2\|\sqrt{\eta}\mathbf{D}^{n+1}\|^2 + \|\sqrt{b}\mathbf{v}^{n+1}\|^2\right) \\
+ 3\Theta\|d_{tt}\mathbf{Q}^n\|^2 + \frac{1}{4}\|d_{tt}\mathbf{v}^n\|^2 + \frac{1}{4}\|\sqrt{K}\nabla d_{tt}\mathbf{Q}^n\|^2 + \frac{1}{4}\|\sqrt{W}d_{tt}\mathbf{Q}^n\|^2 \leq 0.
\end{aligned} \tag{A.6}$$

In particular, (A.4) implies  $E_{\text{BDF2}}^{n+1} \leq E_{\text{BDF2}}^n$  for every  $\tau > 0$ .

*Proof.* In the passive case,  $B_2(\mathbf{f}_\mathbf{v}^n) = 0$  and  $B_2(\mathbf{F}_\mathbf{Q}^n) = 0$ . The SGE–BDF2 update is

$$\begin{cases} D_{2t}\mathbf{v}^{n+1} = -\nabla p^{n+1} + 2\nabla \cdot (\eta\mathbf{D}^{n+1}) - b\mathbf{v}^{n+1} + \zeta^{n+1}B_2(\mathbf{c}_\mathbf{v}^n) - \omega^{n+1}B_2(\mathbf{g}_\mathbf{v}^n), \\ \nabla \cdot \mathbf{v}^{n+1} = 0, \\ D_{2t}\mathbf{Q}^{n+1} = -\Gamma_\mathbf{Q}\mathbf{G}_\mathbf{Q}^{n+1} + \zeta^{n+1}B_2(\mathbf{C}_\mathbf{Q}^n) - \omega^{n+1}B_2(\mathbf{G}_\mathbf{Q}^n). \end{cases} \tag{A.7}$$

Take the  $L^2$  inner product of the first equation in (A.7) with  $\tau\mathbf{v}^{n+1}$  and the  $L^2$  inner product of the third equation in (A.7) with  $\tau\mathbf{G}_\mathbf{Q}^{n+1}$ . The pressure term vanishes because

$$-\tau(\nabla p^{n+1}, \mathbf{v}^{n+1}) = \tau(p^{n+1}, \nabla \cdot \mathbf{v}^{n+1}) = 0.$$

The viscous and drag terms yield

$$2\tau(\nabla \cdot (\eta\mathbf{D}^{n+1}), \mathbf{v}^{n+1}) = -2\tau\|\sqrt{\eta}\mathbf{D}^{n+1}\|^2,$$

and

$$-\tau(b\mathbf{v}^{n+1}, \mathbf{v}^{n+1}) = -\tau\|\sqrt{b}\mathbf{v}^{n+1}\|^2.$$

The tensor dissipation gives

$$-\tau(\Gamma_\mathbf{Q}\mathbf{G}_\mathbf{Q}^{n+1}, \mathbf{G}_\mathbf{Q}^{n+1}) = -\tau\|\sqrt{\Gamma_\mathbf{Q}}\mathbf{G}_\mathbf{Q}^{n+1}\|^2.$$

The SGE terms cancel exactly. Indeed,

$$\begin{aligned}
&\zeta^{n+1} \left[ (\mathbf{v}^{n+1}, B_2(\mathbf{c}_\mathbf{v}^n)) + (\mathbf{G}_\mathbf{Q}^{n+1}, B_2(\mathbf{C}_\mathbf{Q}^n)) \right] \\
&- \omega^{n+1} \left[ (\mathbf{v}^{n+1}, B_2(\mathbf{g}_\mathbf{v}^n)) + (\mathbf{G}_\mathbf{Q}^{n+1}, B_2(\mathbf{G}_\mathbf{Q}^n)) \right] \\
&= \zeta^{n+1}\omega^{n+1} (\|B_2(\mathbf{g}_\mathbf{v}^n)\|^2 + \|B_2(\mathbf{G}_\mathbf{Q}^n)\|^2) \\
&- \omega^{n+1}\zeta^{n+1} (\|B_2(\mathbf{g}_\mathbf{v}^n)\|^2 + \|B_2(\mathbf{G}_\mathbf{Q}^n)\|^2) = 0.
\end{aligned}$$

Adding the two tested equations yields

$$\begin{aligned} & \frac{1}{2} (d_{2t} \mathbf{v}^{n+1}, \mathbf{v}^{n+1}) + \frac{1}{2} (d_{2t} \mathbf{Q}^{n+1}, \mathbf{G}_{\mathbf{Q}}^{n+1}) \\ & = -\tau \left( 2\|\sqrt{\eta} \mathbf{D}^{n+1}\|^2 + \|\sqrt{b} \mathbf{v}^{n+1}\|^2 + \|\sqrt{\Gamma_{\mathbf{Q}}} \mathbf{G}_{\mathbf{Q}}^{n+1}\|^2 \right). \end{aligned} \quad (\text{A.8})$$

By the definition of  $\mathbf{G}_{\mathbf{Q}}^{n+1}$ ,

$$\begin{aligned} & \frac{1}{2} (d_{2t} \mathbf{Q}^{n+1}, \mathbf{G}_{\mathbf{Q}}^{n+1}) \\ & = \frac{1}{2} (d_{2t} \mathbf{Q}^{n+1}, -\nabla \cdot (K \nabla \mathbf{Q}^{n+1}) + W(\mathbf{Q}^{n+1} - \mathbf{Q}_{\star})) \\ & \quad + \frac{1}{2} (d_{2t} \mathbf{Q}^{n+1}, B_2(f_N(\mathbf{Q}^n))) + \frac{\tau \kappa}{4} \|d_{2t} \mathbf{Q}^{n+1}\|^2. \end{aligned} \quad (\text{A.9})$$

Applying (A.1) to the velocity gives

$$\frac{1}{2} (d_{2t} \mathbf{v}^{n+1}, \mathbf{v}^{n+1}) = \frac{1}{4} d_t (\|\mathbf{v}^{n+1}\|^2 + \|B_2(\mathbf{v}^{n+1})\|^2) + \frac{1}{4} \|d_{tt} \mathbf{v}^n\|^2. \quad (\text{A.10})$$

Using integration by parts and the boundary conditions, the linear tensor part satisfies

$$\begin{aligned} & \frac{1}{2} (d_{2t} \mathbf{Q}^{n+1}, -\nabla \cdot (K \nabla \mathbf{Q}^{n+1}) + W(\mathbf{Q}^{n+1} - \mathbf{Q}_{\star})) \\ & = \frac{1}{4} d_t \left( \|\sqrt{K} \nabla \mathbf{Q}^{n+1}\|^2 + \|\sqrt{K} \nabla B_2(\mathbf{Q}^{n+1})\|^2 \right) + \frac{1}{4} \|\sqrt{K} \nabla d_{tt} \mathbf{Q}^n\|^2 \\ & \quad + \frac{1}{4} d_t \left( \|\sqrt{W}(\mathbf{Q}^{n+1} - \mathbf{Q}_{\star})\|^2 + \|\sqrt{W} B_2(\mathbf{Q}^{n+1} - \mathbf{Q}_{\star})\|^2 \right) + \frac{1}{4} \|\sqrt{W} d_{tt} \mathbf{Q}^n\|^2. \end{aligned} \quad (\text{A.11})$$

By (A.3),

$$\begin{aligned} & \frac{1}{2} (d_{2t} \mathbf{Q}^{n+1}, B_2(f_{\text{bulk}}(\mathbf{Q}^n))) \\ & \geq \frac{1}{2} d_{2t} F_{\text{bulk}}(\mathbf{Q}^{n+1}) - \frac{3L_f}{2} \|d_t \mathbf{Q}^{n+1}\|^2 - \frac{3L_f}{2} \|d_t \mathbf{Q}^n\|^2 \\ & = d_t \left( \frac{3}{2} F_{\text{bulk}}(\mathbf{Q}^{n+1}) - \frac{1}{2} F_{\text{bulk}}(\mathbf{Q}^n) \right) - \frac{3L_f}{2} \|d_t \mathbf{Q}^{n+1}\|^2 - \frac{3L_f}{2} \|d_t \mathbf{Q}^n\|^2. \end{aligned} \quad (\text{A.12})$$

Combining (A.8)–(A.12) gives

$$\begin{aligned} & \tilde{E}^{n+1} - \tilde{E}^n + \tau \left( 2\|\sqrt{\eta} \mathbf{D}^{n+1}\|^2 + \|\sqrt{b} \mathbf{v}^{n+1}\|^2 + \|\sqrt{\Gamma_{\mathbf{Q}}} \mathbf{G}_{\mathbf{Q}}^{n+1}\|^2 \right) \\ & \quad + \frac{\tau \kappa}{4} \|d_{2t} \mathbf{Q}^{n+1}\|^2 + \frac{1}{4} \|d_{tt} \mathbf{v}^n\|^2 + \frac{1}{4} \|\sqrt{K} \nabla d_{tt} \mathbf{Q}^n\|^2 + \frac{1}{4} \|\sqrt{W} d_{tt} \mathbf{Q}^n\|^2 \\ & \leq \frac{3L_f}{2} \|d_t \mathbf{Q}^{n+1}\|^2 + \frac{3L_f}{2} \|d_t \mathbf{Q}^n\|^2, \end{aligned} \quad (\text{A.13})$$

where  $\tilde{E}^{n+1}$  denotes (A.5) without the last term  $\left(2\Theta + \frac{3L_f}{2}\right) \|d_t \mathbf{Q}^{n+1}\|^2$ .

The Allen–Cahn stabilization is used through the following square estimate. For the dissipative tensor block, after the SGE contribution has canceled in the summed energy identity,

$$D_{2t} \mathbf{Q}^{n+1} = -\Gamma_{\mathbf{Q}} \mathbf{G}_{\mathbf{Q}}^{n+1}.$$

Consequently,

$$\tau \|\sqrt{\Gamma_{\mathbf{Q}}} \mathbf{G}_{\mathbf{Q}}^{n+1}\|^2 = \frac{1}{4\tau} \left\| \Gamma_{\mathbf{Q}}^{-1/2} d_{2t} \mathbf{Q}^{n+1} \right\|^2.$$

Since  $\Gamma_{\mathbf{Q}} \leq \bar{\Gamma}$ , we obtain

$$\begin{aligned} & \tau \|\sqrt{\Gamma_{\mathbf{Q}}} \mathbf{G}_{\mathbf{Q}}^{n+1}\|^2 + \frac{\tau\kappa}{4} \|d_{2t} \mathbf{Q}^{n+1}\|^2 \\ & \geq \left( \frac{1}{4\tau\bar{\Gamma}} + \frac{\tau\kappa}{4} \right) \|d_{2t} \mathbf{Q}^{n+1}\|^2 \geq \Theta \|d_{2t} \mathbf{Q}^{n+1}\|^2. \end{aligned} \quad (\text{A.14})$$

Using (A.14) in (A.13) gives

$$\begin{aligned} & \tilde{E}^{n+1} - \tilde{E}^n + \Theta \|d_{2t} \mathbf{Q}^{n+1}\|^2 + \tau \left( 2\|\sqrt{\eta} \mathbf{D}^{n+1}\|^2 + \|\sqrt{b} \mathbf{v}^{n+1}\|^2 \right) \\ & + \frac{1}{4} \|d_{tt} \mathbf{v}^n\|^2 + \frac{1}{4} \|\sqrt{K} \nabla d_{tt} \mathbf{Q}^n\|^2 + \frac{1}{4} \|\sqrt{W} d_{tt} \mathbf{Q}^n\|^2 \\ & \leq \frac{3L_f}{2} \|d_t \mathbf{Q}^{n+1}\|^2 + \frac{3L_f}{2} \|d_t \mathbf{Q}^n\|^2. \end{aligned} \quad (\text{A.15})$$

Finally, by (A.2),

$$\|d_{2t} \mathbf{Q}^{n+1}\|^2 = 6\|d_t \mathbf{Q}^{n+1}\|^2 - 2\|d_t \mathbf{Q}^n\|^2 + 3\|d_{tt} \mathbf{Q}^n\|^2. \quad (\text{A.16})$$

Substituting (A.16) into (A.15) and moving all terms to the left-hand side yield

$$\begin{aligned} & \tilde{E}^{n+1} - \tilde{E}^n + \left( 6\Theta - \frac{3L_f}{2} \right) \|d_t \mathbf{Q}^{n+1}\|^2 - \left( 2\Theta + \frac{3L_f}{2} \right) \|d_t \mathbf{Q}^n\|^2 \\ & + 3\Theta \|d_{tt} \mathbf{Q}^n\|^2 + \frac{1}{4} \|d_{tt} \mathbf{v}^n\|^2 + \frac{1}{4} \|\sqrt{K} \nabla d_{tt} \mathbf{Q}^n\|^2 + \frac{1}{4} \|\sqrt{W} d_{tt} \mathbf{Q}^n\|^2 \\ & \leq -2\tau \|\sqrt{\eta} \mathbf{D}^{n+1}\|^2 - \tau \|\sqrt{b} \mathbf{v}^{n+1}\|^2. \end{aligned}$$

Add and subtract  $\left( 2\Theta + \frac{3L_f}{2} \right) \|d_t \mathbf{Q}^{n+1}\|^2$ . The difference of the added terms is precisely the last part of the modified energy (A.5), and the remaining coefficient of  $\|d_t \mathbf{Q}^{n+1}\|^2$  is

$$6\Theta - \frac{3L_f}{2} - \left( 2\Theta + \frac{3L_f}{2} \right) = 4\Theta - 3L_f.$$

This proves (A.6). Finally, (A.4) is equivalent to  $4\Theta \geq 3L_f$ ; hence the modified energy is non-increasing for arbitrary  $\tau > 0$ .  $\square$

**Remark Appendix A.1** The condition, (A.4), is a sufficient condition to ensure the energy stability of the SGE–BDF2 scheme. As in the BDF1 case, such a requirement is mainly introduced to ensure the validity of the theoretical analysis and is not expected to be necessary in practical computations. In practice, the stabilization parameter can be chosen in a more practical way, potentially in conjunction with the time step size, while preserving energy stable behavior.

## References

- [1] C. Dombrowski, L. Cisneros, S. Chatkaew, R. E. Goldstein, J. O. Kessler, Self-Concentration and Large-Scale Coherence in Bacterial Dynamics, *Phys. Rev. Lett.* 93 (9) (2004) 098103.

- [2] C. Becco, N. Vandewalle, J. Delcourt, P. Poncin, Experimental evidences of a structural and dynamical transition in fish school, *Phys. A: Stat. Mech. Appl.* 367 (2006) 487–493.
- [3] W. Bialek, A. Cavagna, I. Giardina, T. Mora, E. Silvestri, M. Viale, A. M. Walczak, Statistical mechanics for natural flocks of birds, *Proc. Natl. Acad. Sci. U.S.A.* 109 (13) (2012) 4786–4791.
- [4] A. Cavagna, A. Cimarelli, I. Giardina, G. Parisi, R. Santagati, F. Stefanini, M. Viale, Scale-free correlations in starling flocks, *Proc. Natl. Acad. Sci. U.S.A.* 107 (26) (2010) 11865–11870.
- [5] T. Sanchez, D. T. N. Chen, S. J. DeCamp, M. Heymann, Z. Dogic, Spontaneous motion in hierarchically assembled active matter, *Nature* 491 (7424) (2012) 431–434.
- [6] J. Kierfeld, K. Frentzel, P. Kraikivski, R. Lipowsky, Active dynamics of filaments in motility assays, *Eur. Phys. J. Spec. Top.* 157 (1) (2008) 123–133.
- [7] A. Majumdar, M. M. Cristina, E. G. Virga, Perspectives in active liquid crystals, *Philos. Trans. R. Soc. A* 372 (2029) (2014) 20130373.
- [8] M. Poujade, E. Grasland-Mongrain, A. Hertzog, J. Jouanneau, P. Chavrier, B. Ladoux, A. Buguin, P. Silberzan, Collective migration of an epithelial monolayer in response to a model wound, *Proc. Natl. Acad. Sci. U.S.A.* 104 (41) (2007) 15988–15993.
- [9] L. Petitjean, M. Reffay, E. Grasland-Mongrain, M. Poujade, B. Ladoux, A. Buguin, P. Silberzan, Velocity Fields in a Collectively Migrating Epithelium, *Biophys. J.* 98 (9) (2010) 1790–1800.
- [10] H. H. Wensink, J. Dunkel, S. Heidenreich, K. Drescher, R. E. Goldstein, H. Löwen, J. M. Yeomans, Meso-scale turbulence in living fluids, *Proc. Natl. Acad. Sci. U.S.A.* 109 (36) (2012) 14308–14313.
- [11] M. C. Marchetti, J. Joanny, S. Ramaswamy, T. Liverpool, J. Prost, M. Rao, R. Simha, Hydrodynamics of soft active matter, *Rev. Mod. Phys.* 85 (3) (2013) 1143–1189.
- [12] S. Ramaswamy, The Mechanics and Statistics of Active Matter, *Annu. Rev. Condens. Matter Phys.* 1 (1) (2010) 323–345.
- [13] J. Toner, Y. Tu, Long-Range Order in a Two-Dimensional Dynamical XY Model: How Birds Fly Together, *Phys. Rev. Lett.* 75 (23) (1995) 4326.
- [14] T. Vicsek, A. Czirók, E. Ben-Jacob, I. Cohen, O. Shochet, Novel Type of Phase Transition in a System of Self-Driven Particles, *Phys. Rev. Lett.* 75 (6) (1995) 1226–1229.
- [15] L. Giomi, A. DeSimone, Spontaneous Division and Motility in Active Nematic Droplets, *Phys. Rev. Lett.* 112 (14) (2014) 147802.
- [16] D. A, T. SP, Y. JM, Defect-mediated morphologies in growing cell colonies, *Physical Review Letters* 117 (4) (2016) 048102.
- [17] L. J. Ruske, J. M. Yeomans, Morphology of Active Deformable 3D Droplets, *Phys. Rev. X.* 11 (2) (2021) 021001.
- [18] R. A. Simha, S. Ramaswamy, Hydrodynamic Fluctuations and Instabilities in Ordered Suspensions of Self-Propelled Particles, *Phys. Rev. Lett.* 89 (5) (2002) 058101.

- [19] Q. Wang, Generalized onsager principle and its applications, in: X. you Liu (Ed.), *Frontiers and Progress of Current Soft Matter Research*, Springer Nature, 2020, Ch. 3, pp. 101–132.
- [20] J. F. Joanny, F. Julicher, K. Kruse, J. Prost, Hydrodynamic theory for multi-component active polar gels, *New Journal of Physics* 9(11) (2007) 422.
- [21] J. Prost, F. Julicher, J. Joanny, Active gel physics, *Active gel physics* 11 (2015) 111.
- [22] J. L. Guermond, P. Mineev, J. Shen, An overview of projection methods for incompressible flows, *Comput. Methods Appl. Mech. Eng.* 195 (44) (2006) 6011–6045.
- [23] J. L. Guermond, L. Quartapelle, A Projection FEM for Variable Density Incompressible Flows, *J. Comput. Phys.* 165 (1) (2000) 167–188.
- [24] J. L. Guermond, A. Salgado, A splitting method for incompressible flows with variable density based on a pressure Poisson equation, *J. Comput. Phys.* 228 (8) (2009) 2834–2846.
- [25] R. H. Nochetto, A. J. Salgado, I. Tomas, A diffuse interface model for two-phase ferrofluid flows, *Comput. Methods Appl. Mech. Eng.* 309 (2016) 497–531.
- [26] J. Shen, X. Yang, Numerical approximations of Allen-Cahn and Cahn-Hilliard equations, *Discrete Contin. Dyn. Syst.* 28 (4) (2010) 1669–1691.
- [27] J. Zhao, Q. Wang, X. Yang, Numerical Approximations to a New Phase Field Model for Immiscible Mixtures of Nematic Liquid Crystals and Viscous Fluids, *Comput. Methods Appl. Mech. Eng.* 310 (2016) 77–97.
- [28] D. J. Eyre, Unconditionally Gradient Stable Time Marching the Cahn-Hilliard Equation, *Mater. Res. Soc. Symp. Proc.* 529 (1) (1998) 39–46.
- [29] Z. Guan, J. S. Lowengrub, C. Wang, S. M. Wise, Second order convex splitting schemes for periodic nonlocal Cahn–Hilliard and Allen–Cahn equations, *J. Comput. Phys.* 277 (2014) 48–71.
- [30] X. Yang, Linear, first and second-order, unconditionally energy stable numerical schemes for the phase field model of homopolymer blends, *J. Comput. Phys.* 327 (2016) 294–316.
- [31] X. Yang, J. Zhao, Q. Wang, Numerical Approximations for a phase field dendritic Growth Model Based on the Invariant Energy Quadraticization Approach, *Int. J. Numer. Methods Eng.* 110 (3) (2017) 2790300.
- [32] J. Zhao, X. Yang, Y. Gong, Q. Wang, A Novel Linear Second Order Unconditionally Energy-stable Scheme for a Hydrodynamic Q-tensor Model of Liquid Crystals, *Comput. Methods Appl. Mech. Eng.* 318 (2017) 803–825.
- [33] X. Yang, H. Yu, Efficient Second Order Unconditionally Stable Schemes for a Phase Field Moving Contact Line Model Using an Invariant Energy Quadraticization Approach, *SIAM J. Sci. Comput.* 40 (3) (2018) B889–B914.
- [34] J. Shen, J. Xu, J. Yang, The scalar auxiliary variable (SAV) approach for gradient flows, *J. Comput. Phys.* 353 (2018) 407–416.
- [35] J. Shen, J. Xu, J. Yang, A New Class of Efficient and Robust Energy Stable Schemes for Gradient Flows, *SIAM Rev.* 61 (3) (2019) 474–506.

- [36] Q. Hong, J. Li, Q. Wang, Supplementary Variable Method for Structure-Preserving Approximations to Partial Differential Equations with Deduced Equations, *Appl. Math. Lett.* 110 (2020) 106576.
- [37] Y. Gong, Q. Hong, Q. Wang, Supplementary Variable Method for Thermodynamically Consistent Partial Differential Equations, *Comput. Methods Appl. Mech. Eng.* 381 (2021) 113746.
- [38] Q. Hong, Q. Wang, Y. Gong, Efficient High-Order Supplementary Variable Methods for Thermodynamically Consistent Partial Differential Equations, *Comput. Methods Appl. Mech. Eng.* 416 (2023) 1163062023.
- [39] X. Yang, Numerical approximations of the Navier–Stokes equation coupled with volume-conserved multi-phase-field vesicles system: Fully-decoupled, linear, unconditionally energy stable and second-order time-accurate numerical scheme, *Comput. Methods Appl. Mech. Eng.* 375 (2021).
- [40] X. Li, J. Shen, Z. Liu, New sav-pressure correction methods for the navier-stokes equations: stability and error analysis, *Math. Comput.* 91 (2022) 141–167.
- [41] X. Gu, Q. Wang, Skew Gradient Embedding for Thermodynamically Consistent Systems, *arXiv:2509.18601 [math.NA]* (2025).
- [42] S. Eidnes, L. Li, S. Sato, Linearly implicit structure-preserving schemes for Hamiltonian systems, *J. Comput. Appl. Math.* 387 (2021) 112489.
- [43] M. Doi, S. F. Edwards, *The PTheory of Polymer Dynamics*, Oxford University Press, Oxford, 1986.
- [44] P.-G. de Gennes, J. Prost, *The Physics of Liquid Crystals*, 2nd Edition, Oxford University Press, Oxford, 1993.
- [45] Q. Wang, Biaxial steady states and their stability in shear flows of liquid crystal polymers, *J. Rheol.* 41 (5) (1997) 943–970.
- [46] H. Zhou, H. Wang, Q. Wang, M. G. Forest, Characterization of stable kinetic equilibria of rigid, dipolar rod ensembles for coupled dipole-dipole and excluded-volume potentials, *Nonlinearity* 20 (2007) 277–297.
- [47] X. Yang, *Modelling and Simulations of Active Liquid Crystals*, Thesis, Nankai University (2014).
- [48] D. Marenduzzo, E. Orlandini, M. Cates, J. Yeomans, Steady-state hydrodynamic instabilities of active liquid crystals: Hybrid lattice Boltzmann simulations, *Phys. Rev. E* 76 (3) (2007) 031921.
- [49] V. R. J. JF, P. J, Spontaneous flow transition in active polar gels, *Europhysics Letters* 70 (3) (2005) 404.
- [50] A. N. Beris, B. J. Edwards, *Thermodynamics of Flowing Systems with Internal Microstructures*, Oxford University Press, Oxford, 1994.
- [51] J. Zhao, Q. Wang, Semi-discrete energy-stable schemes for a tensor-based hydrodynamic model of nematic liquid crystal flows, *J. Sci. Comput.* 68 (2016) 1241–1266.

- [52] N. Lu, C. Wang, L. Zhang, Z. Zhang, Decoupled and energy stable schemes for phase-field surfactant model based on mobility operator splitting technique, *J. Comput. Appl. Math.* 459 (2025) 116365.
- [53] L. Wang, H. Yu, An energy stable linear diffusive Crank-Nicolson scheme for the Cahn-Hilliard gradient flow, *J. Comput. Appl. Math.* 377 (2020) 112880.
- [54] X. Feng, T. Tang, J. Yang, Stabilized Crank-Nicolson/Adams-Bashforth schemes for phase field models, *E. Asian. J. Appl. Math.* 3 (1) (2013) 59–80.
- [55] T. Tang, J. Yang, Implicit-explicit scheme for the Allen-Cahn equation preserves the maximum principle, *J. Comput. Math.* 34 (2016) 471–481.
- [56] T. Tang, Z. Qiao, Efficient numerical methods for phase-field equations (in Chinese), *Sci. Sin. Math.* 50 (2020) 775–794.
- [57] E. Celledoni, V. Grimm, R. McLachlan, D. McLaren, D. O’Neale, B. Owren, G. Quispel, Preserving energy resp. dissipation in numerical PDEs using the “Averaged Vector Field” method, *J. Comput. Phys.* 231 (2012) 6770–6789.
- [58] G. Quispel, D. McLaren, A new class of energy-preserving numerical integration methods, *J. Phys. A: Math. Theor.* 41 (2008) 045206.
- [59] H. Li, Y. Wang, An averaged vector field Legendre spectral element method for the nonlinear Schrödinger equation, *Int. J. Comput. Math.* 94 (2017) 1196–1218.
- [60] J. Cai, J. Hong, Y. Wang, Y. Gong, Two energy-conserved splitting methods for three-dimensional time-domain Maxwell’s equations and the convergence analysis, *SIAM J. Numer. Anal.* 53 (2015) 1918–1940.
- [61] H. Li, Y. Wang, M. Qin, A Sixth order averaged vector field method, *J. Comput. Math.* 34 (2016) 479–498.
- [62] F. Huang, J. Shen, Stability and error analysis of a class of high-order imex schemes for navier-stokes equations with periodic boundary conditions, *SIAM J. Numer. Anal.* 59 (6) (2021) 2926–2954.
- [63] M. Dahlby, B. Owren, A general framework for deriving integral preserving numerical methods for PDEs, *SIAM J. Sci. Comput.* 33 (2011) 2318–2340.
- [64] Q. Hong, Q. Wang, Thermodynamically consistent hybrid computational models for fluid-particle interactions, *J. Comput. Phys.* 513 (2024) 113147.
- [65] Q. Hong, Q. Wang, Hybrid hydrodynamic models for active elastic particles driven by self-generated force couples, *Phys. Fluids* 37 (2025) 031923.
- [66] Y. Gong, J. Zhao, Q. Wang, Second order fully discrete energy stable methods on staggered grids for hydrodynamic phase field models of binary viscous fluids, *SIAM J. Sci. Comput.* 40 (2018) B528–B553.
- [67] S. P. Vanka, Block-Implicit multigrid solution of Navier-Stokes equations in primitive variables, *J. Comput. Phys.* 65 (1986) 138–158.